

NASA TM X-55608

AN INTERFEROMETRIC RANGING SYSTEM

GPO PRICE \$ _____

CFSTI PRICE(S) \$ _____

Hard copy (HC) 2.50

Microfiche (MF) .75

ff 653 July 65

BY
DIANE M. TILLSON

SEPTEMBER 1966



GODDARD SPACE FLIGHT CENTER

GREENBELT, MD.

N67 11380

FACILITY FORM 602

(ACCESSION NUMBER)

75

(PAGES)

TMX-55608

(NASA CR OR TMX OR AD NUMBER)

(THRU)

(CODE)

(CATEGORY)

AN INTERFEROMETRIC RANGING SYSTEM

by

Diane Marie Tillson

September 1966

Approved:

H. H. Plotkin

H. H. Plotkin
Head, Optical Systems Branch

R. J. Coates

Robert J. Coates
Chief, Advanced Development Div.

Goddard Space Flight Center
Greenbelt, Maryland

TABLE OF CONTENTS

	Page
LIST OF TABLES	iv
LIST OF FIGURES	v
ACKNOWLEDGMENTS	vii
ABSTRACT	viii
I. INTRODUCTION.	1
A. Historical Survey of Ranging Techniques	1
B. Description of the Proposed Ranging System.	5
II. THEORY.	9
A. Brief Analysis of Lasing and Mode Selection.	9
B. Analysis of Signal Strength as a Function of Length . . .	12
C. Analysis of Accuracy Limitations	18
III. EXPERIMENTAL PROCEDURES	24
A. Ranging System	24
1. Dual-Mode Gas Laser.	24
2. Beam Collimation and the Michelson Interferometer.	29
3. Detection Circuit to Monitor Beat Note Signal	32
B. Measurements and Results.	32
1. Determination of the Laser Difference Frequency Stability	38
2. Determination of Null Points and Data Reduction . . .	43
3. Results.	53
C. Alternate High Accuracy Ranging System	54
1. Method of Frequency Stabilization of the Laser	54
2. Determination of Null Points and Data Reduction . . .	61
3. Results.	68
IV. CONCLUSION	69
V. LITERATURE CITED.	70

LIST OF TABLES

		Page
Table I	List and Short Description of Packaged Equipment Used in the Ranging System	37
Table II	Tabulation of Laser Beat-Note Frequency Drift—Long Term Drift	38
Table III	Beat-Note Frequency of the Laser Monitored on a Frequency Counter	42
Table IV	Data Giving Four Null Positions	44
Table V	Statistical Analysis of Null A	49
Table VI	Statistical Analysis of Null B	50
Table VII	Statistical Analysis of Null C	51
Table VIII	Statistical Analysis of Null D	52
Table IX	Data Giving Null Positions [Ranging system utilizing stabilized laser].	63
Table X	Statistical Analysis of Null A'	66
Table XI	Statistical Analysis of Null B'	67

LIST OF FIGURES

		Page
Figure 1	Geodimeter — Principle of Operation.	2
Figure 2	Interferometric Ranging System. Principle of Operation — Counts the Interference Fringes from the Optical Signal	4
Figure 3	Experimental Laser Ranging System	7
Figure 4	Spectral Linewidth Factors in the He-Ne Laser	10
Figure 5	Helium-Neon Energy Level Diagram	11
Figure 6	I_{RMS} as a Function of the Cosine (kL).	19
Figure 7	Helium-Neon Gas Laser	25
Figure 8	Photograph of the Helium-Neon Laser	26
Figure 9	TEM ₀₀ Uniphase Intensity Pattern.	27
Figure 10	Long-Radius Mirrors Resonator Configuration Giving Uniphase Wavefronts.	28
Figure 11	Arrangement to Collimate the Laser Output	30
Figure 12	Michelson Interferometer	31
Figure 13	Spectral Sensitivity Characteristic of a Phototube Having S-17 Response.	33
Figure 14	Circuit to Monitor Beat-Note Signal Strength.	34
Figure 15	a. In-Phase Signal Strength.	35
	b. Out-of-Phase Signal Strength.	36
Figure 16	Circuit to Determine Long Term Stability of the Laser Beat Note.	39
Figure 17	Photograph of Frequency Drift of Laser Beat-Note after One Hour.	40
Figure 18	Distribution of Readings for Null A	45
Figure 19	Distribution of Readings for Null B	46

	Page
Figure 20	Distribution of Readings for Null C 47
Figure 21	Distribution of Readings for Null D 48
Figure 22	Locking Circuit Used to Stabilize the Self-Beat of the Laser 57
Figure 23	Laser Stabilization Loop 58
Figure 24	Hemispherical Resonator Configuration Giving Uniphase Wavefronts. 59
Figure 25	Experimental Ranging System with Stabilized Laser . 62
Figure 26	Distribution of Readings for Null A' 64
Figure 27	Distribution of Readings for Null B' 65

ACKNOWLEDGMENTS

The author wishes to express her appreciation to Dr. Henry H. Plotkin, Messrs. Nelson McAvoy, Peter O. Minott, and Michael Fitzmaurice for their assistance and guidance.

N67-11380

ABSTRACT

The need for an accurate linear measuring system in the range of one hundred meters has resulted in the investigation of potential laser applicability. This paper analyzes an interferometric type ranging system which utilizes a continuous-wave laser. Theoretical analysis shows that one can utilize the difference frequency between adjacent TEM longitudinal modes of a c-w laser to make accurate distance measurements. Equations are developed to establish mathematically the relation between phase information, which results from the photo-mixing of two monochromatic light beams, and the path lengths of these two signals.

The validity of this idea is verified experimentally. Measurements which were accurate to a half millimeter were obtained using this ranging system. The accuracy of the system is limited by the system's noise level and by the laser stability.

Author

PART I
INTRODUCTION

A. Historical Survey of Ranging Techniques

At present there are three basic ranging techniques: mechanical, interferometric, and radar. The first method, the mechanical approach, compares a physical length standard (e.g., a gage block) with the unknown distance. The second method, interferometry, evaluates the unknown length in terms of the wavelength of electromagnetic radiation. The third method, radar, employs a burst or pulse of radiation which propagates along the path to be measured; the necessary back-up electronic equipment records the time it takes for the emitted radiation to return.

Of these three techniques, the interferometric method is best suited to measure intermediate distances up to several kilometers with high accuracy. In contrast, mechanical standards are practical only for distances of a few centimeters and are themselves calibrated by means of interferometry; the radar approach yields high percent accuracy only for distances of several hundred kilometers.

Interferometric length measurements made in metrology labs use the spectrum line of monochromatic light. Limitations due to coherence length restricts the range of this type of system to a few centimeters.

A modified Michelson interferometry measuring system, called a geodimeter, operates as shown in Figure 1. This instrument projects a light beam modulated at approximately 30 MHz/s over the unknown distance (up to twenty-five kilometers) to a passive reflector. The light

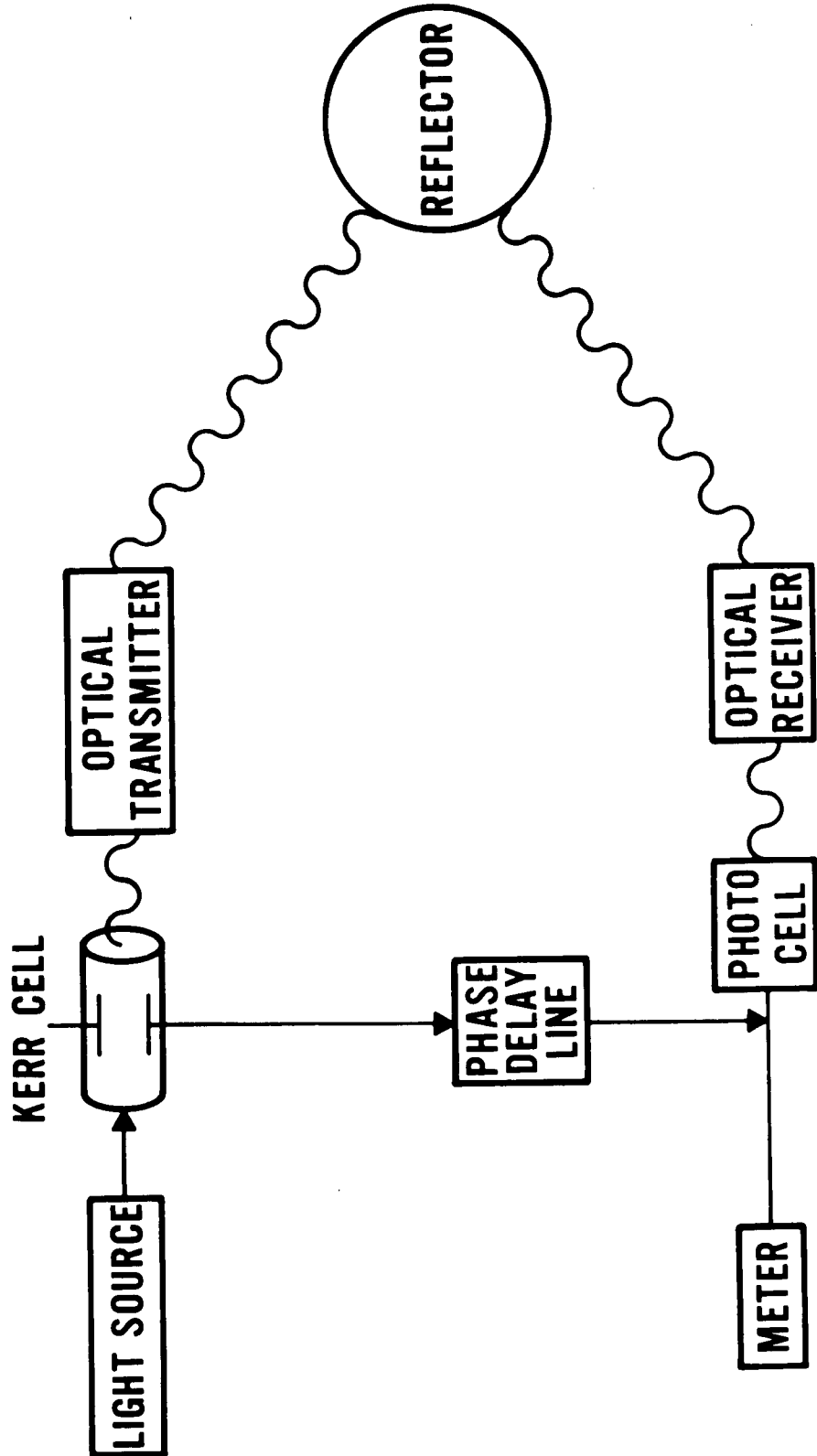


Figure 1 - Geodimeter - Principle of Operation

beam is modulated utilizing the electro-optic properties of a Kerr Cell. An adjustable electric delay line inserted between the Kerr Cell and the phototube makes it possible to determine the phase relation between the transmitted and received light pulses. When the correct adjustment has been made, a null reading is obtained and converted to a distance measurement.

The inherent limitation of the geodimeter as a method to measure intermediate distances is its lack of precision. Typical error associated with this type of instrument is ± 10 millimeters; added to this absolute error of the system is the error $\pm 2 \times 10^{-6}$ of the distance measured.¹

A similar instrument, the tellurometer, utilizes the accuracy of microwave-measuring techniques. This type of instrument operates on principles similar to radar; it determines distance from the time required for a radiowave to travel to and from the point being measured. Like the geodimeter, it derives its accuracy from measuring transit time as phase delays at several ranging frequencies. The limitation of this method is its lack of precision over a few kilometers. Error associated with this instrument is ± 3 centimeters; added to this is the error $\pm 3 \times 10^{-6}$ of the distance measured.⁷

The author knows of one interferometric ranging technique utilizing the laser.² This system is seen in Figure 2. A helium-neon gas laser is the source of a coherent beam of radiation which falls on a partially silvered diagonal mirror. This serves to split the single beam into two parts; one part is reflected to a fixed Mirror A and back to the

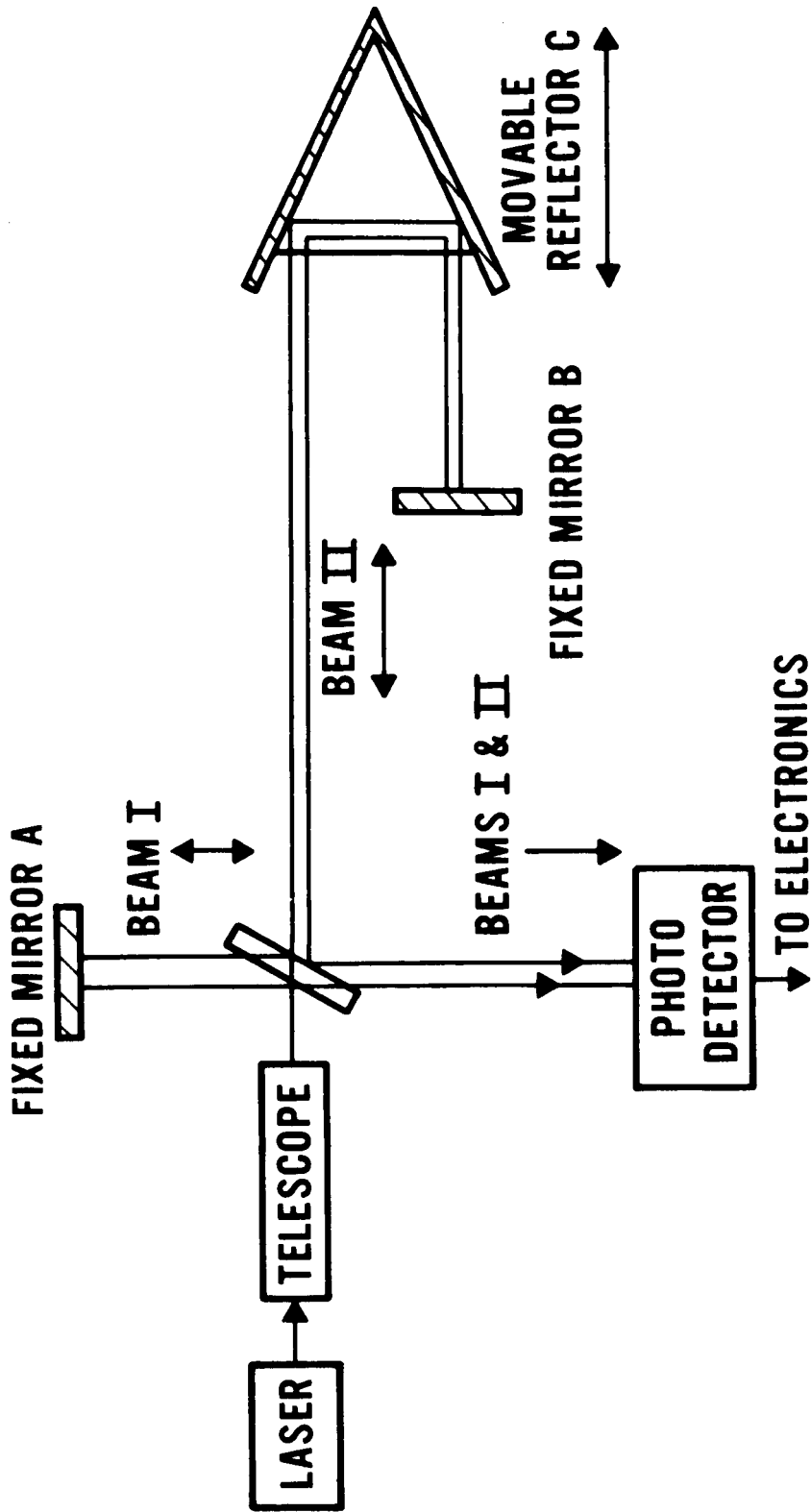


Figure 2 - Interferometric Ranging System. Principle of Operation - Counts the Interference Fringes from the Optical Signal

detector. The other part of the beam is transmitted to a movable Reflector C which directs it to the photodetector.

The movable Reflector C shown in Figure 2 is actually a trihedral prism which consists of three mutually perpendicular reflecting surfaces. This corner cube has the property that any light ray striking it and being reflected at any face will return parallel to its original direction with a slight vertical or horizontal displacement; also, the path length through the prism remains constant.

When the two beams recombine, interference effects are observed. If the paths of the two beams are equal or differ by an even integral multiple of π , the light is in phase; however, if one path differs from the other by any other amount, they are observed to be out of phase. Optical fringes result from the interference effects; they are produced by moving the reflector through the length to be measured. These fringes are then counted and converted into centimeters of travel by electronic equipment.

B. Description of the Proposed Ranging System

This paper presents a new method of measuring intermediate distances. A continuous-wave laser is used for the light source because it produces sharp spectral lines closely spaced in frequency. When light from a c-w laser impinges on a square-law detector, the output of the detector gives the difference frequencies, or inherent "beat-notes," between adjacent modes.¹⁰

A theoretical analysis shows that the difference frequency between the adjacent TEM_{ooq} and TEM_{ooq+1} modes of a c-w laser can be

utilized to make accurate distance measurements; that is, it can be established mathematically that the phase information of a signal resulting from the photomixing of two monochromatic light beams is dependent on their relative path lengths. A physical system has been devised to verify experimentally the validity of this argument.

The actual system is as shown in Figure 3. The helium-neon gas laser emits two adjacent TEM longitudinal modes at frequencies ω_1 and ω_2 . This beam of plane polarized light is transmitted parallel to the axis of the interferometer. The beams are then divided by a beam splitter. One part goes to Mirror A where it is reflected back to the detector; the second part of the beam is transmitted to a movable Mirror B and is then reflected back to the beam splitter where it is reflected to the photomultiplier. This square-law detector responds to the difference of these two frequencies $\omega_1 - \omega_2$. When the two interferometer arms are equal or differ by an integral multiple of λ of the difference frequency, the beat notes are in phase; however by moving Mirror B, the difference frequency moves in and out of phase with the beat note of the first arm.

The light beams from the two arms of the interferometer impinge on the photomultiplier. The resultant signal is then fed to a spectrum analyzer which is tuned to the beat frequency. Changes in phase can thus be monitored; that is, as the beat from leg two moves in and out of phase with the beat from leg one, variations in signal strength are observed in terms of height variations of the signal on the spectrum analyzer. Therefore the location of null points, points of 180° phase

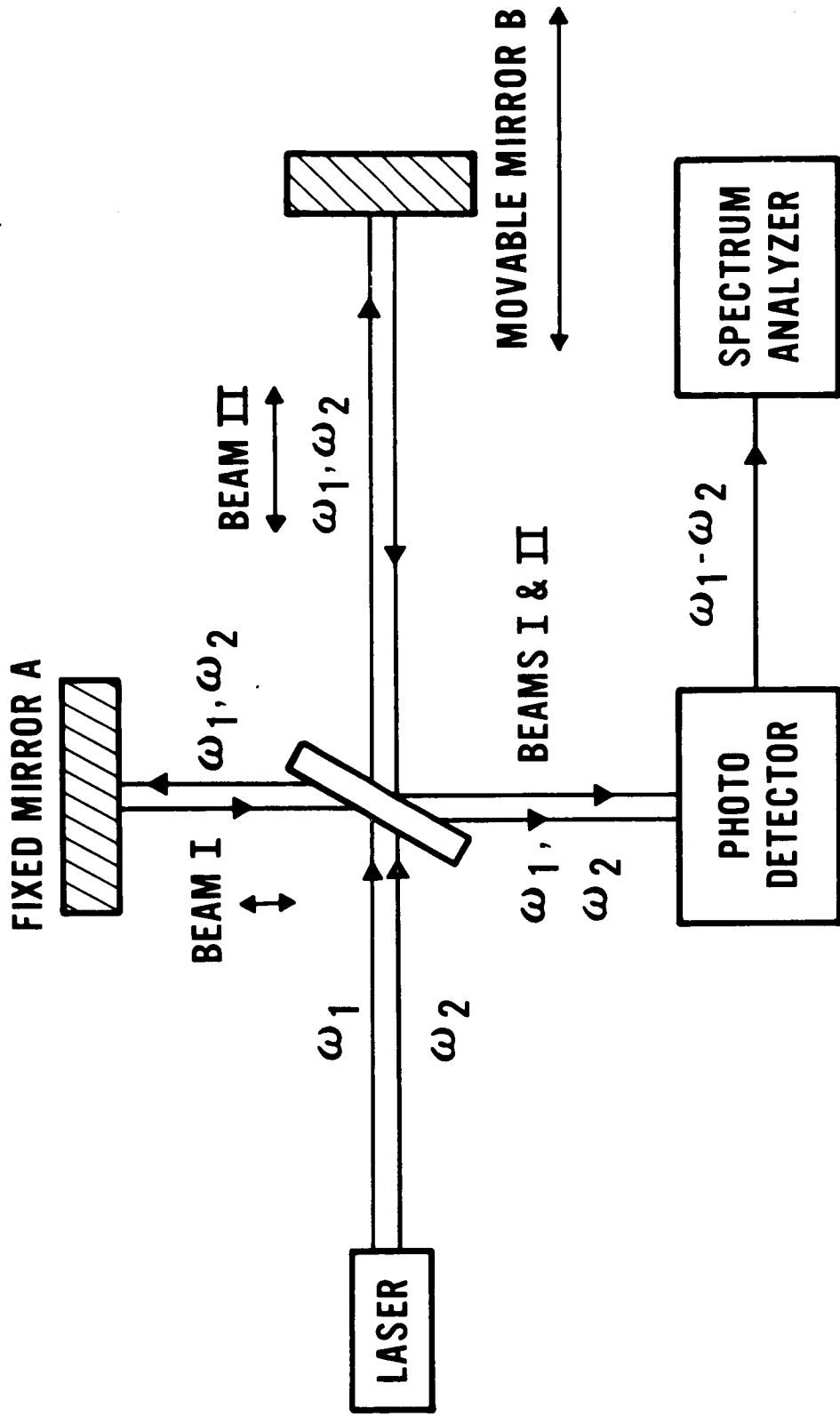


Figure 3 - Experimental Laser Ranging System

difference, can be accurately measured and precisely correlated to changes in distance.

PART II

THEORY

A. Brief Analysis of Lasing and Mode Selection

As stated in the introduction, a Michelson interferometer is used to make intermediate range measurements (refer to Figure 3). The He-Ne gas laser emits two adjacent TEM_{ooq} and TEM_{ooq+1} modes at frequencies ω_1 and ω_2 . These frequencies, as seen in Figure 4, are determined by three factors: the natural linewidth of the stimulated atomic transition; the broadening, primarily Doppler broadening, of this natural linewidth; and the location and linewidth of the resonator modes.

The laser oscillation arises from a population inversion of the energy levels of the neon atomic system located inside a high Q optical resonator; this results in the laser oscillation. The energy level diagram shown in Figure 5 illustrates the atomic processes involved in producing coherent oscillation in a c-w helium-neon gas laser.

Helium atoms are raised to the metastable excited state 20.61 electron volts above the ground state. Nearly coincident in energy is the $3s_2$ state of neon, 20.66 electron volts above the neon ground state.* It is known that if two atoms possess excited states with nearly equal energies above the ground states, then transfer of excitation may take

*Following well-established but inconsistent precedents, the standard Russell-Saunders notation is used to designate levels of helium; the historical semi-empirical Paschen symbols are used for the levels of neon.

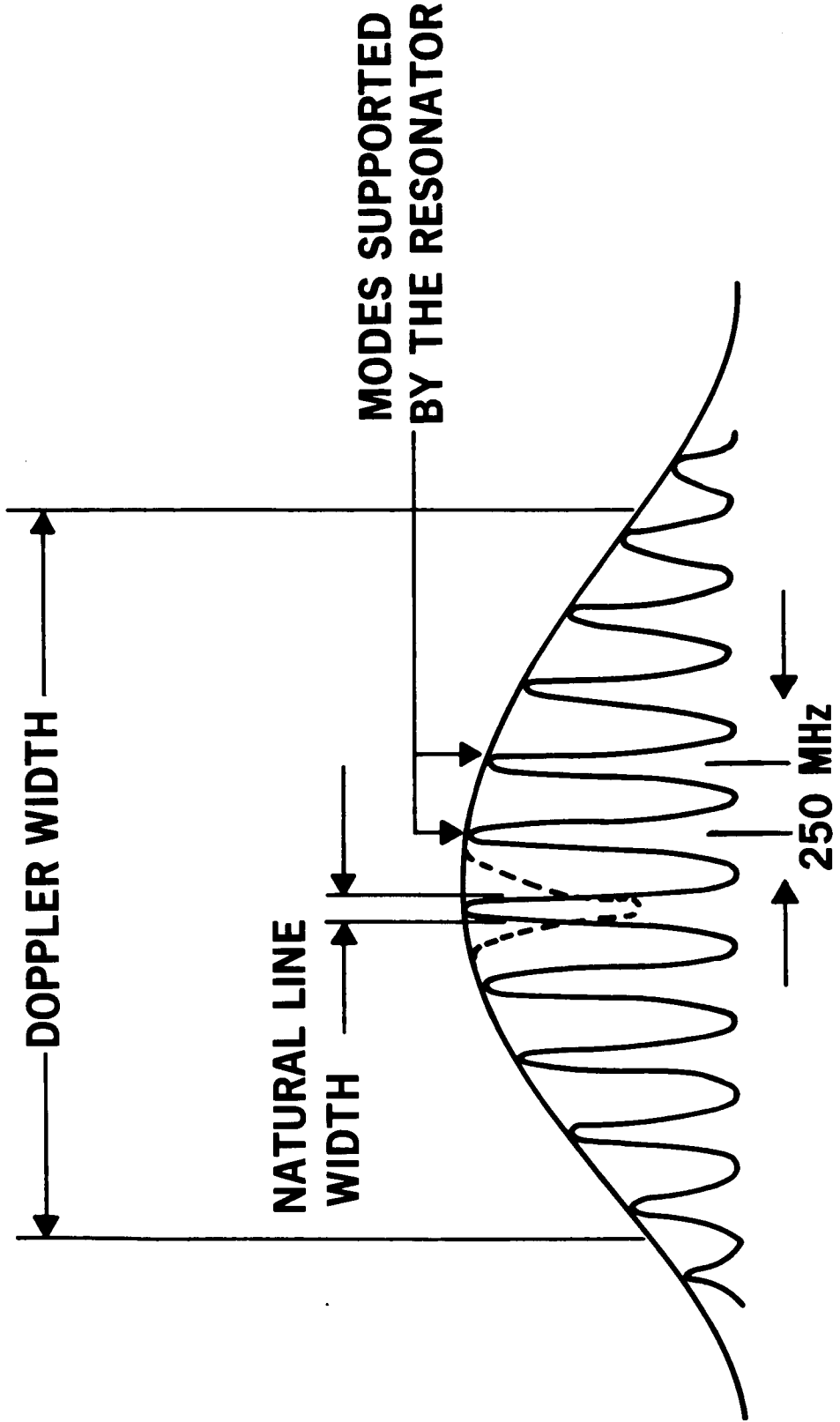


Figure 4 - Spectral Linewidth Factors in the He-Ne Laser

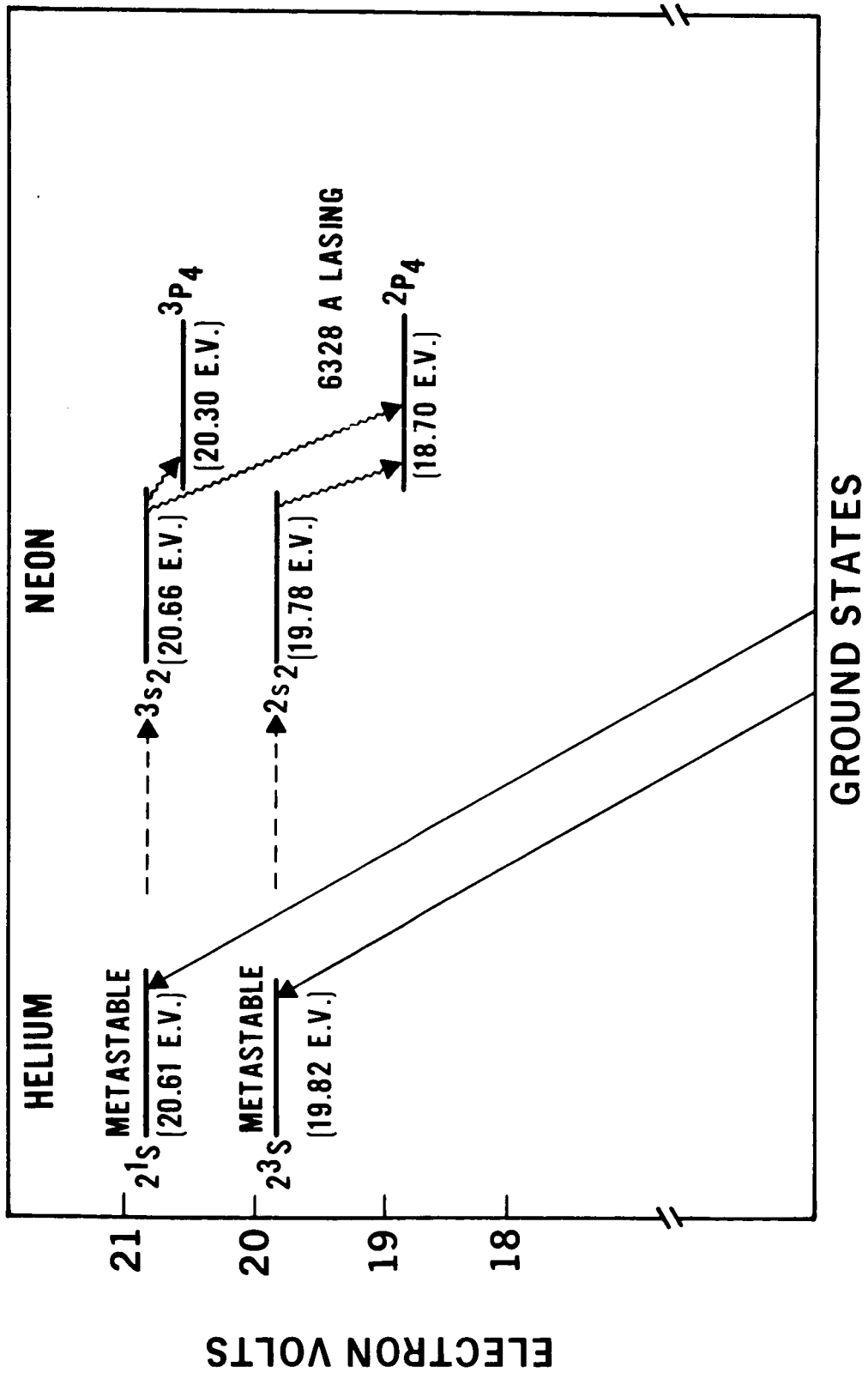


Figure 5 - Helium-Neon Energy Level Diagram

place between an excited atom of one species and a ground state of the other. This type of process is particularly effective in one direction if one of the two excited states is metastable. Thus energy exchange collisions occur between the excited helium atoms and the ground state neon atoms. Through this process, the neon atoms are raised to the excited $3s_2$ state and the helium atoms return to the ground state with the small difference in energy taken up by thermal motion.

This action leads to population inversion; that is, the preferential population of the neon $3s_2$ level relative to the $2p_4$ level. The atomic system thus assumes the characteristics of negative resistance or gain at the transition wavelength of 6328 angstroms. A neon atom undergoing the transition from the $3s_2$ level to the $2p_4$ level will emit a photon having an energy of 6328 angstroms.¹¹ In this case, the resonant cavity is adjusted such that it supports only two modes of oscillation, ω_1 and ω_2 , within the Doppler broadened linewidth of the transition.

B. Analysis of Signal Strength as a Function of Length

The author developed the following theory to firmly establish the relationship of signal strength to the length L to be measured.

The electric field at the frequency ω_i ($i = 1,2$) which has propagated a distance x from the front face of the laser is:

$$E_i \cos (\omega_i t + k_i x + \phi_i) \quad (1)$$

where k_i the wave number, $= 2\pi/\lambda_i$

E_i is the maximum electric field intensity at frequency ω_i , and ϕ_i is the phase angle at the front face of the laser.

The total electric field impinging on the photomultiplier from the two arms of the interferometer is:

$$\begin{aligned} E = & E_1^{(1)} \cos (\omega_1 t + k_1 x^{(1)} + \phi_1) + E_1^{(2)} \cos (\omega_1 t + k_1 x^{(2)} + \phi_1) \\ & + E_2^{(1)} \cos (\omega_2 t + k_2 x^{(1)} + \phi_2) + E_2^{(2)} \cos (\omega_2 t + k_2 x^{(2)} + \phi_2) \quad , \quad (2) \end{aligned}$$

where the subscripts distinguish between the two adjacent modes of the laser and the superscripts distinguish between the two arms of the interferometer.

The output current from the photodetector is:⁶

$$\begin{aligned} I &= I^{(1)} + I^{(2)} \\ &= \frac{e\eta G}{\hbar\bar{\omega}} \left[P^{(1)}(x, t) + P^{(2)}(x, t) \right] \quad (3-a) \end{aligned}$$

where $P^{(i)}(x, t)$ represents the impinging radiant power on the photomultiplier from the i^{th} arm,

η is the quantum efficiency of the detector,

G is the photomultiplier tube gain,

$\hbar = \frac{h}{2\pi}$ (h is Planck's constant),

e is the electronic charge, and

$$\bar{\omega} = \frac{\omega_1 + \omega_2}{2} .$$

The relation between power flow and electric field strength is:⁸

$$\vec{P}^{(i)} = \vec{E}^{(i)} \times \vec{H}^{(i)} = E^{(i)2} \sqrt{\mu/\epsilon} A \quad (4)$$

where $\sqrt{\mu/\epsilon}$ is the impedance of free space, and

A is the detector area.

Therefore the current flow from the square-law detector is:

$$I = I^{(1)} + I^{(2)} \quad (3-b)$$

where

$$I^{(1)} = \frac{e\eta GA \sqrt{\mu/\epsilon}}{\hbar\omega} \left[E_1^{(1)} \cos(\omega_1 t + k_1 x^{(1)} + \phi_1) + E_2^{(1)} \cos(\omega_2 t + k_2 x^{(1)} + \phi_2) \right]^2$$

and

$$I^{(2)} = \frac{e\eta GA \sqrt{\mu/\epsilon}}{\hbar\omega} \left[E_1^{(2)} \cos(\omega_1 t + k_1 x^{(2)} + \phi_1) + E_2^{(2)} \cos(\omega_2 t + k_2 x^{(2)} + \phi_2) \right]^2$$

Assuming equal electric field intensities from the two modes, the expression for $I^{(1)}$ can be expanded to the following form:

$$\begin{aligned}
 I^{(1)} = & \frac{e\eta GA \sqrt{\mu/\epsilon}}{\hbar\bar{\omega}} E^{(1)2} \left\{ \frac{1}{2} + \frac{\cos 2(\omega_1 t + k_1 x^{(1)})}{2} \right. \\
 & + \cos(\omega t + kx^{(1)} - \phi_2) + \cos[(\omega_1 + \omega_2)t + (k_1 + k_2)x^{(1)} + \phi_2] \\
 & \left. + \frac{1}{2} + \frac{\cos 2(\omega_2 t + k_2 x^{(1)} + \phi_2)}{2} \right\} \quad (5)
 \end{aligned}$$

where $k = k_1 - k_2$

$\omega = \omega_1 - \omega_2$, and

ϕ_1 , the phase angle of E_1 at the laser face, $\equiv 0$.

Frequencies which are higher than the photomultiplier response time, $1/\tau$, result in the d-c components of the output current. Examination of Equation (5) shows these d-c terms to be:

$$\begin{aligned}
 I_{d-c}^{(1)} = & \frac{e\eta G \sqrt{\mu/\epsilon} AE^{(1)2}}{\hbar\bar{\omega}} \frac{1}{\tau} \int_0^\tau \left\{ 1 + \frac{\cos 2(\omega_1 t + k_1 x^{(1)})}{2} \right. \\
 & + \cos[(\omega_1 + \omega_2)t + (k_1 + k_2)x^{(1)} + \phi_2] \\
 & \left. + \frac{\cos 2(\omega_2 t + k_2 x^{(1)} + \phi_2)}{2} \right\} d\tau \quad (6)
 \end{aligned}$$

These d-c components reduce to the form:

$$I_{d-c}^{(1)} = \frac{e\eta GA E^{(1)2} \sqrt{\mu/\epsilon}}{\hbar \bar{\omega}} \quad (7)$$

which is constant both in time and in space.

Therefore the total output current of the photomultiplier resulting from arm one is:

$$I^{(1)} = \frac{\sqrt{\mu/\epsilon} e\eta GA E^{(1)2}}{\hbar \bar{\omega}} \left[\cos(\omega t + kx^{(1)} - \phi_2) \right] + I_{d-c}^{(1)} \quad (8)$$

This reduces the expression for tube current from arm one to:

$$I^{(1)} = \frac{E^{(1)2} e\eta AG \sqrt{\mu/\epsilon}}{\hbar \bar{\omega}} \left[\sin(\omega t + \phi^{(1)}) \right] + I_{d-c}^{(1)} \quad (9)$$

where

$$\phi^{(1)} = \tan^{-1} \frac{\cos(kx^{(1)} - \phi_2)}{\sin(kx^{(1)} - \phi_2)}$$

or

$$\phi^{(1)} = \frac{\pi}{2} - kx^{(1)} - \phi_2 \equiv kx^{(1)} + \phi'$$

In a similar way, the expression for the tube current from arm two can be shown to be:

$$I^{(2)} = \frac{E^{(2)2} e\eta AG \sqrt{\mu/\epsilon}}{\hbar \bar{\omega}} \left[\sin(\omega t + \phi^{(2)}) \right] + I_{d-c}^{(2)} \quad (10)$$

where

$$\phi^{(2)} = \tan^{-1} \frac{\cos(kx^{(2)} - \phi_2)}{\sin(kx^{(2)} - \phi_2)}$$

or

$$\phi^{(2)} = \pi/2 - kx^{(2)} - \phi_2 \equiv \phi' + kx^{(2)} .$$

Therefore the total output current from the photomultiplier is:

$$\begin{aligned} I &= I^{(1)} + I^{(2)} \\ &= A_1 + A_1 \sin(\omega t + kx^{(1)} + \phi') + A_2 + A_2 \sin(\omega t + kx^{(2)} + \phi') \quad , (11) \end{aligned}$$

where

$$A_1 = \frac{e\eta GA \sqrt{\mu/\epsilon}}{\hbar \bar{\omega}} E^{(1)2} ,$$

and

$$A_2 = \frac{e\eta GA \sqrt{\mu/\epsilon}}{\hbar \bar{\omega}} E^{(2)2} .$$

Ignoring the d-c level since it is constant in time, the output current can then be reduced to the form:

$$I = \sqrt{A_1^2 + A_2^2 + 2A_1 A_2 \cos kL} \sin(\omega t + \phi'') \quad (12)$$

where

$$L = x_2 - x_1 ,$$

and

$$\phi'' = \tan^{-1} \frac{A_1 \cos (kx^{(1)} - \phi') + A_2 \cos (kx^{(2)} - \phi')}{A_1 \sin (kx^{(1)} - \phi') + A_2 \sin (kx^{(2)} - \phi')} .$$

Obtaining the root-mean-square of the periodic component yields:

$$I_{RMS} = \frac{1}{2} \sqrt{2} [A_1^2 + A_2^2 + 2A_1 A_2 \cos kL]^{1/2} . \quad (13)$$

Analysis of Equation (13) shows that I_{RMS} varies as a function of the cosine of the length measured. It is therefore possible to correlate distance travelled with I_{RMS} measured. The I_{RMS} has a maximum value whenever (kL) is an even integral multiple of π ; and it has a minimum value whenever (kL) is an odd integral multiple of π (see Figure 6). It can further be seen that the distance between the points of maximum and minimum current output is independent of the ratio of A_1 to A_2 . The equality of the two beams hitting the photo-cell merely distinguishes more clearly the maximum and minimum points; for example, in the limit of a noise-free system the minimum would go to zero for the case $A_1 = A_2$.

C. Analysis of Accuracy Limitations

The limitations in the accuracy of this ranging system can be seen from the following considerations. The two factors which limit the

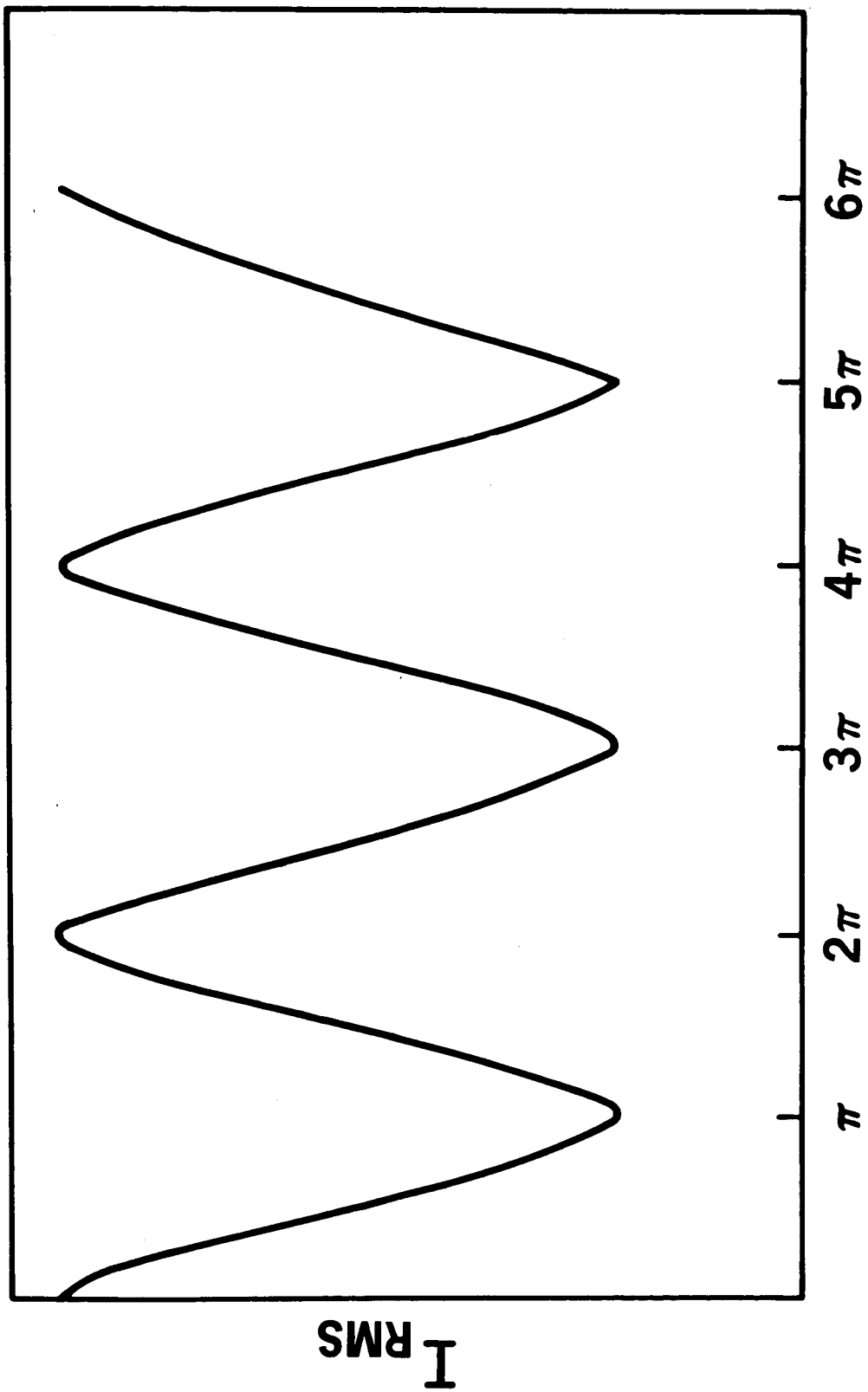


Figure 6 - I_{RMS} as a Function of the Cosine (kL)

precision measurement of L are:

1. current variations due to noise in the system, and
2. variations in the alternating current components caused by instability of the beatnote between the adjacent TEM_{00q} and TEM_{00q+1} modes.

The noise in the system is primarily due to shot noise; this results from random fluctuations of the d-c level of the light impinging on the photomultiplier and also from the spectrum analyzer. The RMS fluctuation current due to shot noise is given by the following relationship:⁹

$$[\bar{I}_{\Delta f}^2]^{1/2} = [2e i_d \Delta f]^{1/2} , \quad (14)$$

where i_d is the combination of current fluctuations resulting from the d-c level of the incoming signal and from noise current in the spectrum analyzer, and

Δf is the bandpass of the measuring circuit.

When the signal current is just equal to this RMS fluctuation current (that is, the signal-to-noise ratio is one), the condition of minimum signal detection is imposed. The uncertainty ΔL in determining L under this condition can be found by equating the RMS signal current at a null or minima with the RMS current fluctuations due to shot noise:

$$[A_1^2 + A_2^2 + 2A_1 A_2 \cos k(L \pm \Delta L)]^{1/2} = [2e i_d \Delta f]^{1/2} . \quad (15)$$

Solving this equation leads to the following expression for the uncertainty in L at a minima due to noise:

$$L \pm \Delta L = \frac{1}{k} \cos^{-1} \left[\frac{e i_d B \bar{h} \bar{\omega} \epsilon}{E^{(1)2} E^{(2)2} e^2 \eta^2 A^2 G^2 \mu} - \frac{E^{(1)2}}{2E^{(2)2}} - \frac{E^{(2)2}}{2E^{(1)2}} \right]. \quad (16)$$

The amount of error introduced in measuring L from the instability of the difference frequency between the two modes can be found from the following two relationships:

$$\left. \frac{\partial I_{\text{RMS}}}{\partial \omega} \right|_{L_{\text{null}}} \Delta \omega = \Delta i_{\omega} \quad (17-a)$$

$$\left. \frac{\partial I_{\text{RMS}}}{\partial L} \right|_{\omega_{\text{null}}} \Delta L = \Delta i_L \quad (17-b)$$

Fluctuations in current due to variations in ω result in uncertainty in L.

Thus

$$\Delta i_{\omega} = \Delta i_L \quad (18-a)$$

or

$$\frac{\partial I_{\text{RMS}}}{\partial \omega} \Delta \omega = \frac{\partial I_{\text{RMS}}}{\partial L} \Delta L \quad (18-b)$$

This leads to the following expression for ΔL

$$\Delta L = \frac{L}{\omega} \Delta \omega \quad (19)$$

The relation of the beat note frequency ω to the cavity length of the resonator can be easily described. For each resonance appearing at frequency ν_n another resonance exists at the frequency J_{n+1} . From the relation $\nu = c/\lambda$, it is seen that

$$\nu_n = \frac{c}{2d/n} \quad (20-a)$$

$$\nu_{n+1} = \frac{c}{2d/(n+1)}, \quad (20-b)$$

where d is the spacing between the reflectors, and n refers to the number of modes.

Combining these two equations leads to the following expression for the difference frequency:

$$\Delta\nu = \frac{c}{2d} \quad (21-a)$$

or

$$\omega = \frac{c}{\pi d} \quad (21-b)$$

The above derivation is valid for only TEM₀₀ modes; this implies no angular misalignment of the end reflectors. Thus any change in the distance between the mirrors of the cavity must be in the axial direction, not in tilt, for the derivation to be valid.

From the examination of the two limitations to precision measurements, it is seen that the shot noise due to the I_{d-c} component of the

signal is an inherent limitation of the system. The amount of error introduced by instability of the difference frequency can be minimized by maintaining a constant length of the end-reflectors.

PART III
EXPERIMENTAL PROCEDURES

A. Ranging System

An experimental ranging system was devised to test the validity of the preceding theory. Figure 3 shows the basic physical system employed.

1. Dual-Mode Gas Laser

The laser shown in Figures 7 and 8 was a helium-neon gas laser with visible output at 6328 \AA . The instrument consisted of a He-Ne plasma tube and quartz mirrors mounted at the ends of a heavy aluminum coaxial cylindrical housing. The end mirrors were adjusted so that the cavity supported at least two modes, TEM_{00q} and TEM_{00q+1} , pictured in Figure 9. The resonator, the large radius mirror configuration, produced uniphase wavefronts; this type of wavefront has the same phase across its entire surface (i.e., there are no 180° phase reversals or nodes in the wavefront) and the intensity pattern of the wavefront has approximately a Gaussian fall-off. As shown in Figure 10, this resonator consists of two spherical mirrors that have a radius on the order of ten to twenty times the length of the resonator. The advantage of the large radius mirror configuration is that the maximum number of excited atoms in the laser are used; thus there is a high output power. However the mirror alignment is critical for this type of resonator.

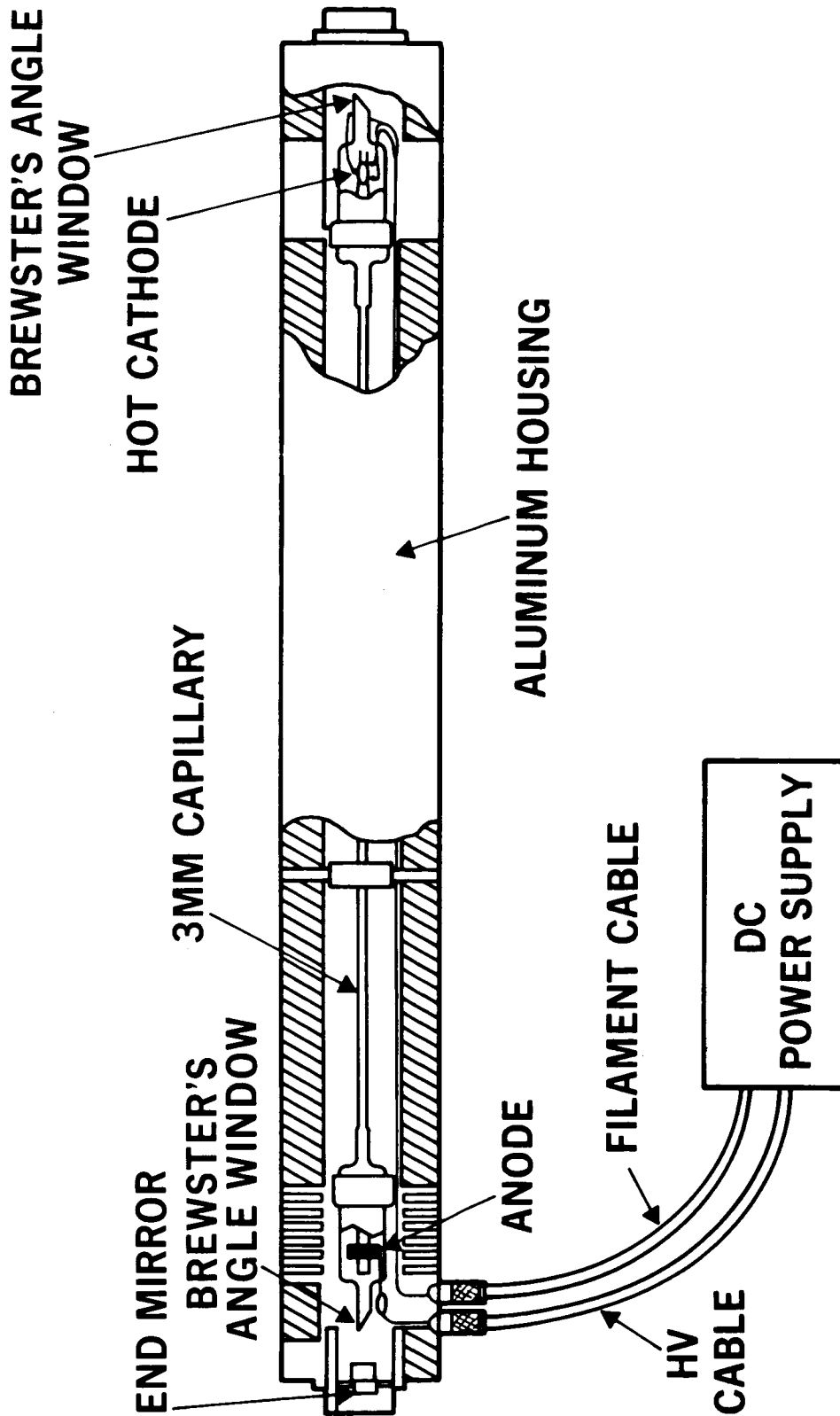


Figure 7 - Helium-Neon Gas Laser

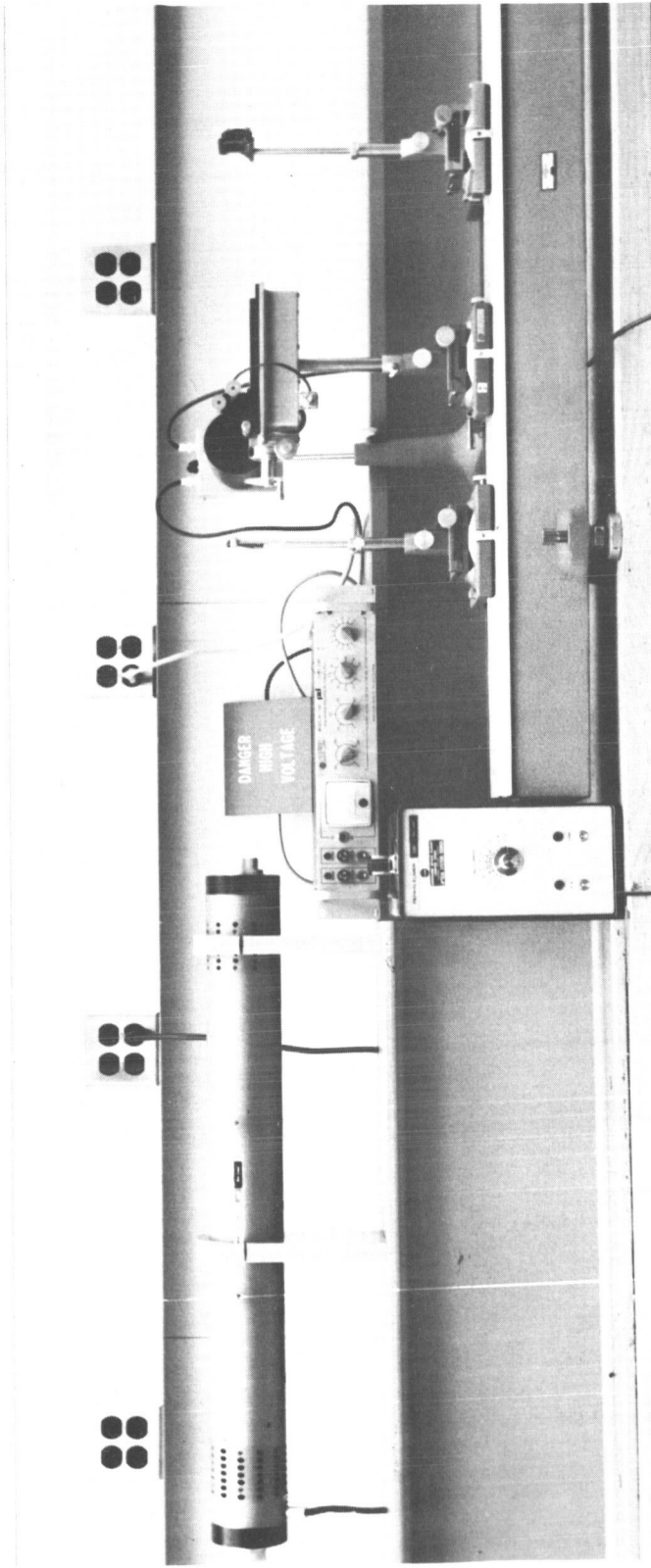


Figure 8 - Photograph of the Helium-Neon Laser

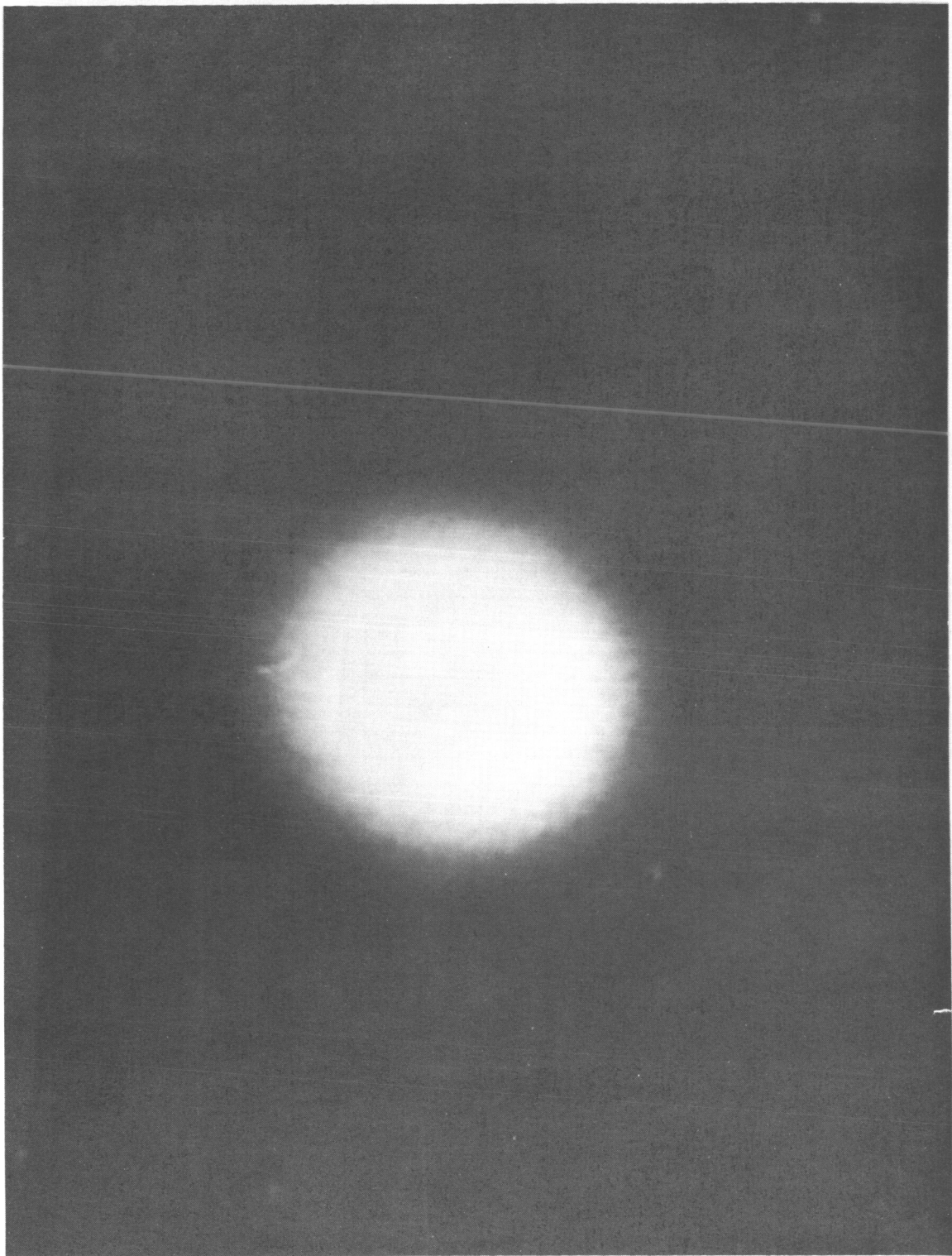


Figure 9 - TEM_{00} . Uniphase Intensity Pattern

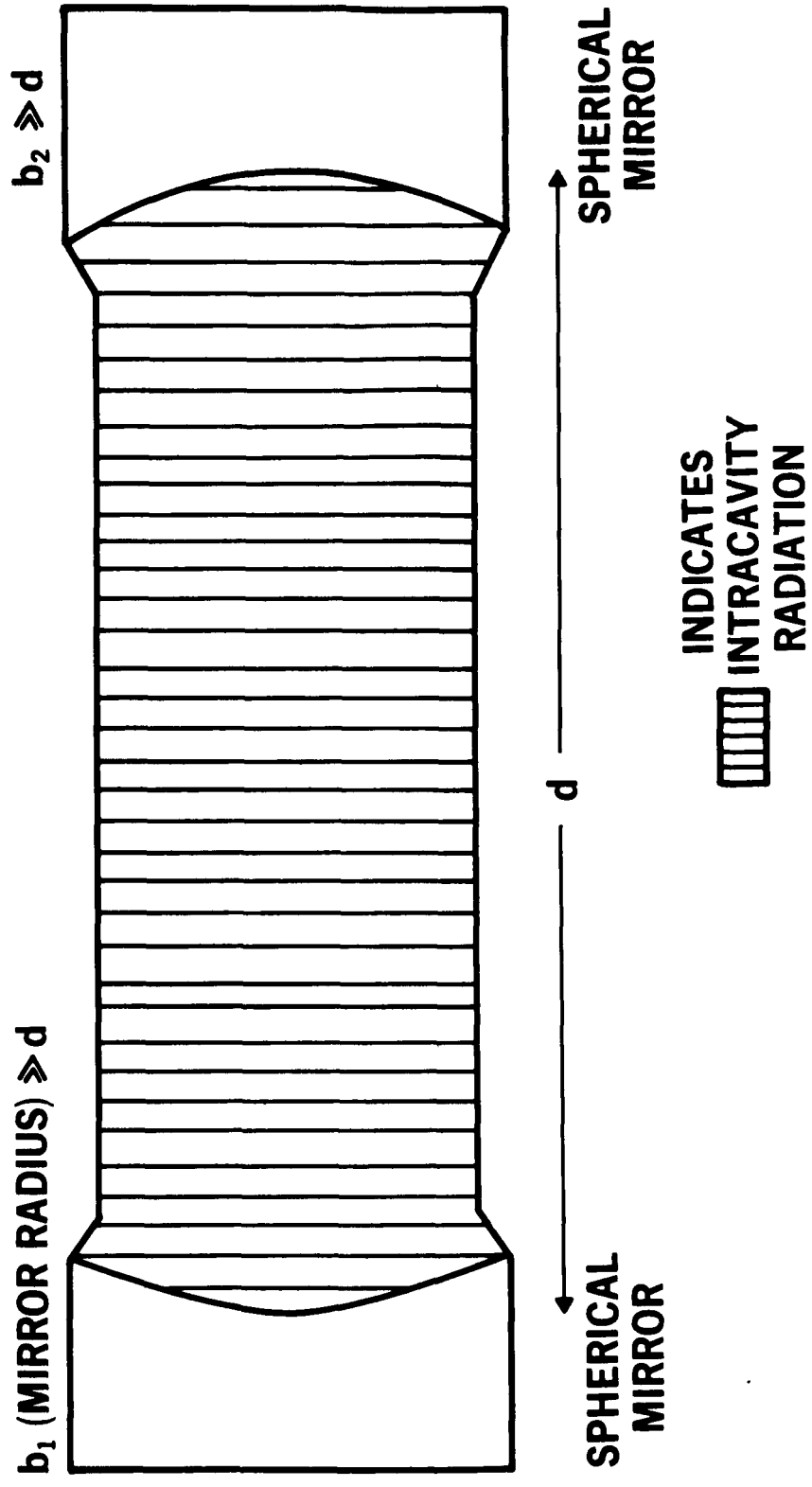


Figure 10 - Long-Radius Mirrors Resonator Configuration Giving Uniphase Wavefronts

2. Beam Collimation and the Michelson Interferometer

The adjacent TEM_{00q} and TEM_{00q+1} modes emitted from the laser are plane polarized (i.e., all the light is vibrating parallel to a plane through the axis of the beam) due to the fact that the plasma tube has Brewster angle windows. The beam emerging from the front end of the laser is then collimated by using two converging lens as seen in Figure 11. After having been brought to a focus by the eye-piece, the light from the diffraction pattern is allowed to propagate further; it then illuminates a much larger lens which in turn collimates the light. This arrangement is the simple astronomical telescope used in reverse.

The beam is then transmitted parallel to the axis of the Michelson Interferometer. This type of interferometer is based on the division of amplitude; the wave front is divided by partial reflection and the two wave fronts maintain their original width but have reduced amplitudes.⁵ The arrangement is shown schematically in Figure 12. The optical parts consist of two highly polished plane mirrors M_1 and M_2 and a plane-parallel plate of glass G . The back side of plate G is silvered so that light coming from the laser is divided into a reflected and a transmitted beam of equal intensity. The light reflected normally from mirror M_1 passes through G a third time and arrives at the photomultiplier as shown. The light reflected from mirror M_2 is reflected from the surface of G and into the photomultiplier.

The entire Michelson interferometer is mounted on an optical bench calibrated to read position accurately to a tenth of a millimeter. Mirror M_1 is mounted on a movable slide in order that the path difference of the light beams could be varied and accurately measured.

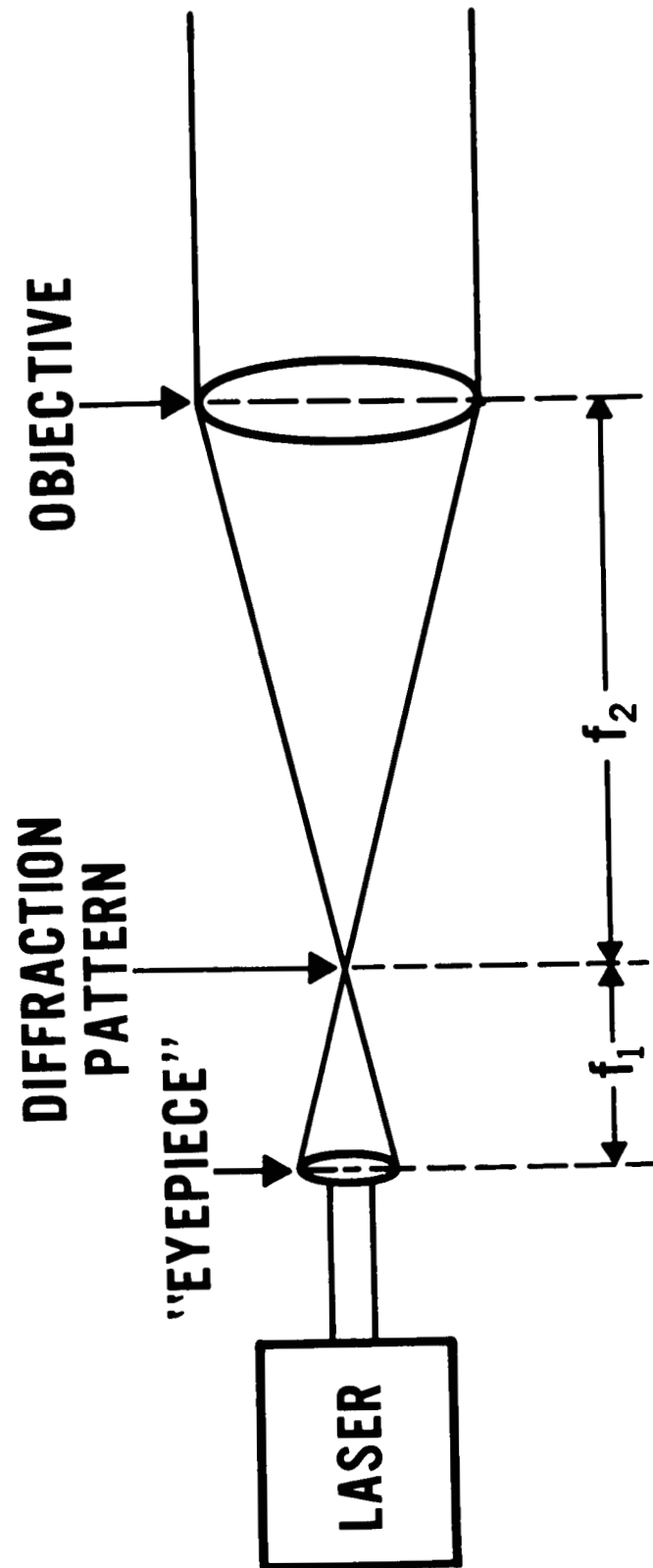


Figure 11 - Arrangement to Collimate the Laser Output

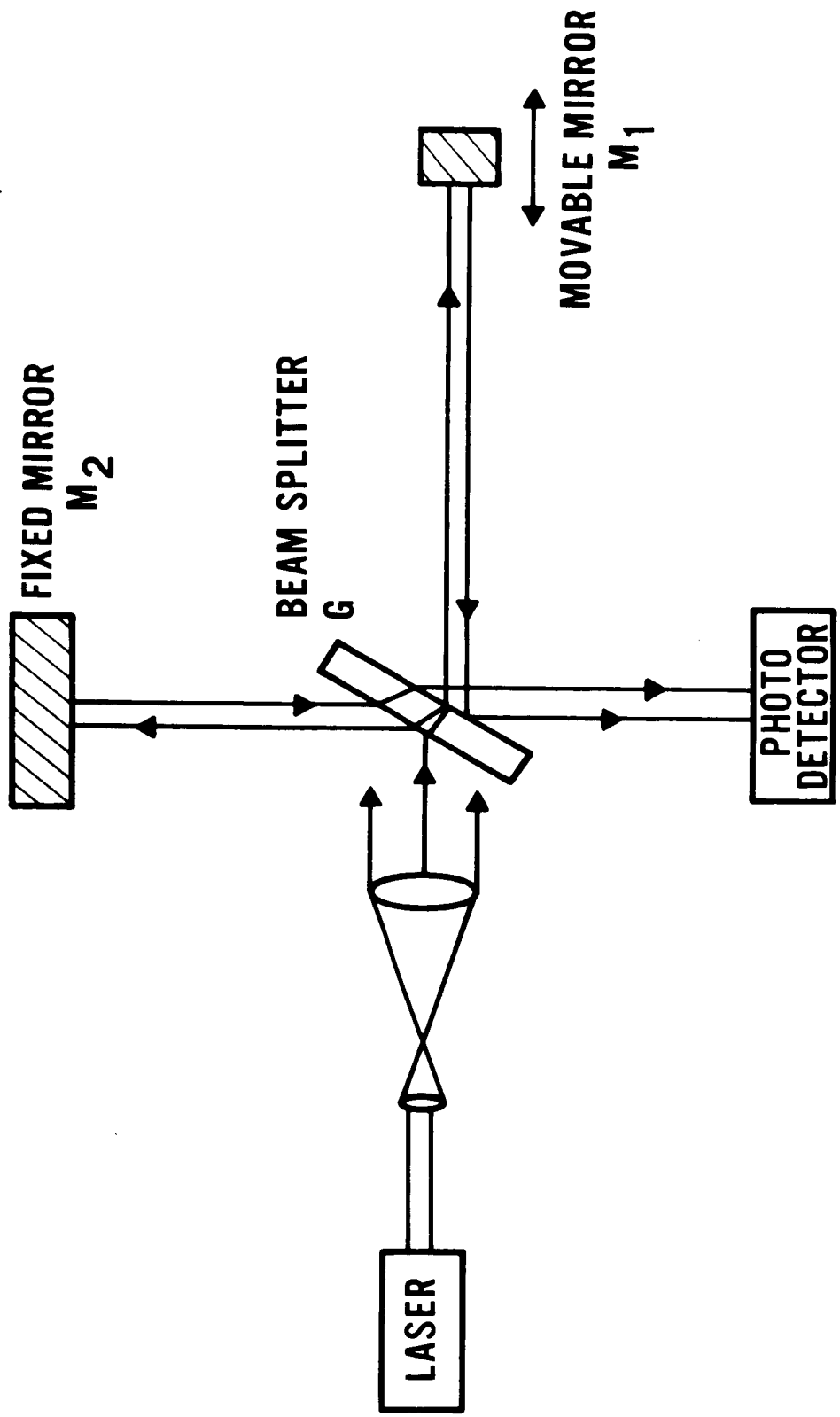


Figure 12 - Michelson Interferometer

3. Detection Circuit to Monitor Beat Note Signal

The light from the two arms of the interferometer impinged on an RCA 7029 photomultiplier. This tube has an S-17 spectral response; the spectral sensitivity characteristic of a phototube having this particular response is shown in Figure 13. The response time of this square-law detector is such that the a-c component of the output current is due only to the difference frequency, $\omega_1 - \omega_2$, and higher harmonics of the impinging light.

As seen in Figure 14, the output current was then fed into a spectrum analyzer which was used as a receiver in this particular case. The instrument was tuned to 170 MHz, the beat-note frequency, with an adjustable bandwidth of approximately 50kHz

Varying the path difference between the two arms of the interferometer resulted in an intensity variation of the 170 MHz signal displayed on the spectrum analyzer. Figure 15-a shows the signal strength displayed on the spectrum analyzer when the two signals were in phase; Figure 15-b shows the signal strength when the two signals were 180° out of phase. Thus one could measure null points to a tenth of a millimeter by monitoring the 170 MHz signal strength displayed on the spectrum analyzer. This provided an experimental check on the validity of the interpretation of Equation (13).

B. Measurements and Results

The experimental ranging unit was arranged as described in the preceding section (see Figure 3). A list and short description of the packaged equipment used in this ranging system is given in Table I.

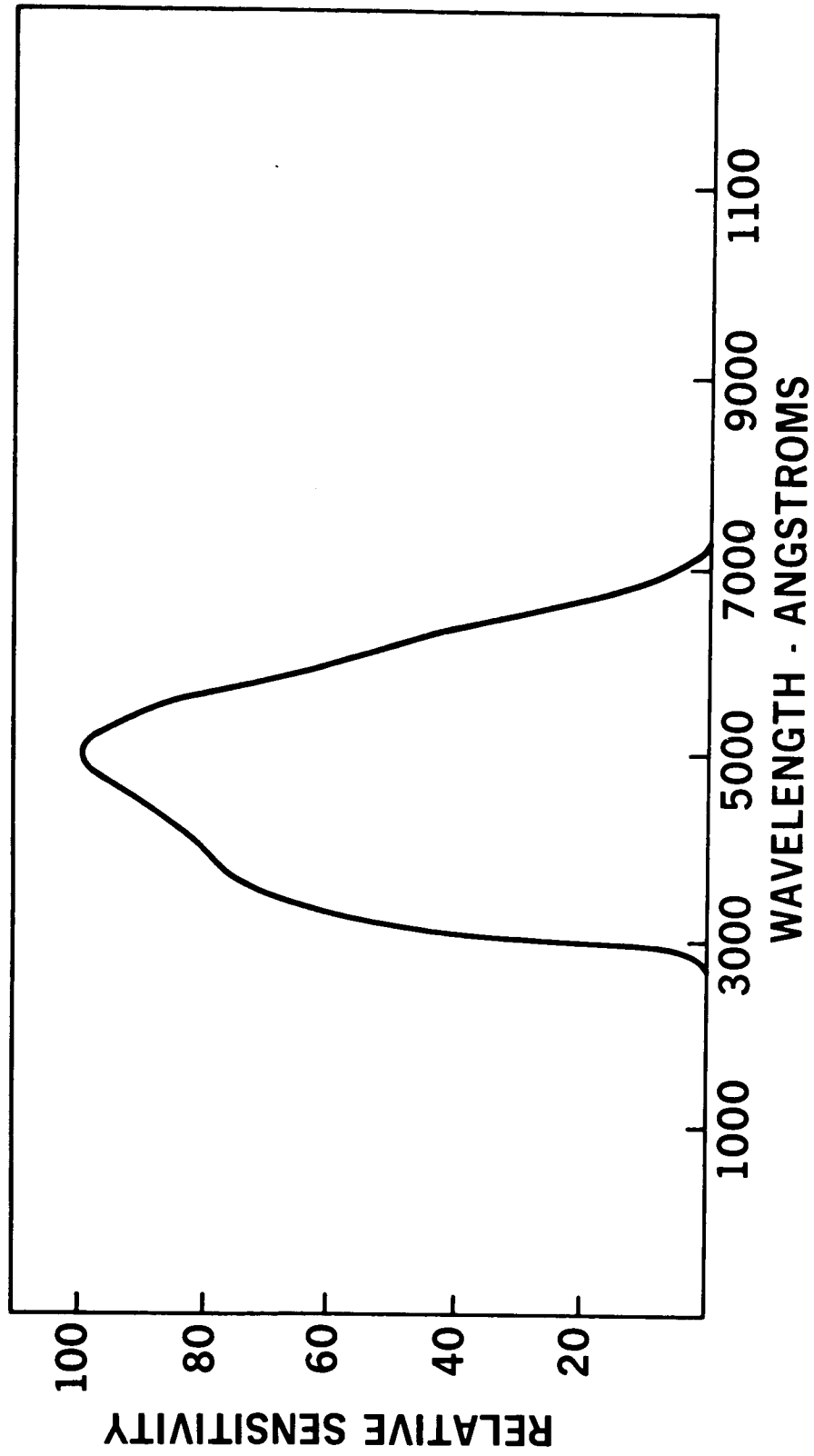


Figure 13 - Spectral Sensitivity Characteristic of a Phototube Having S-17 Response

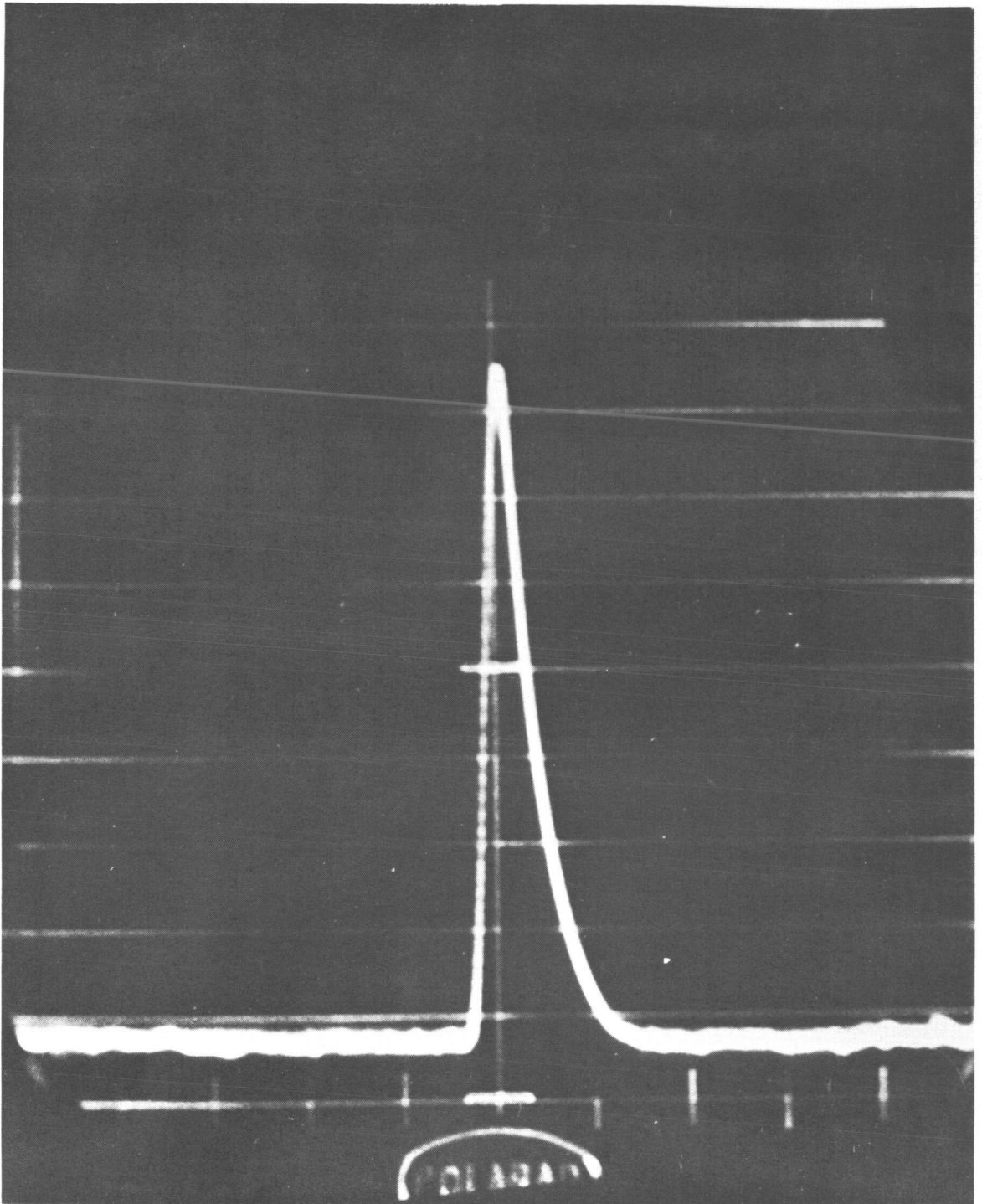


Figure 15a - In-Phase Signal Strength

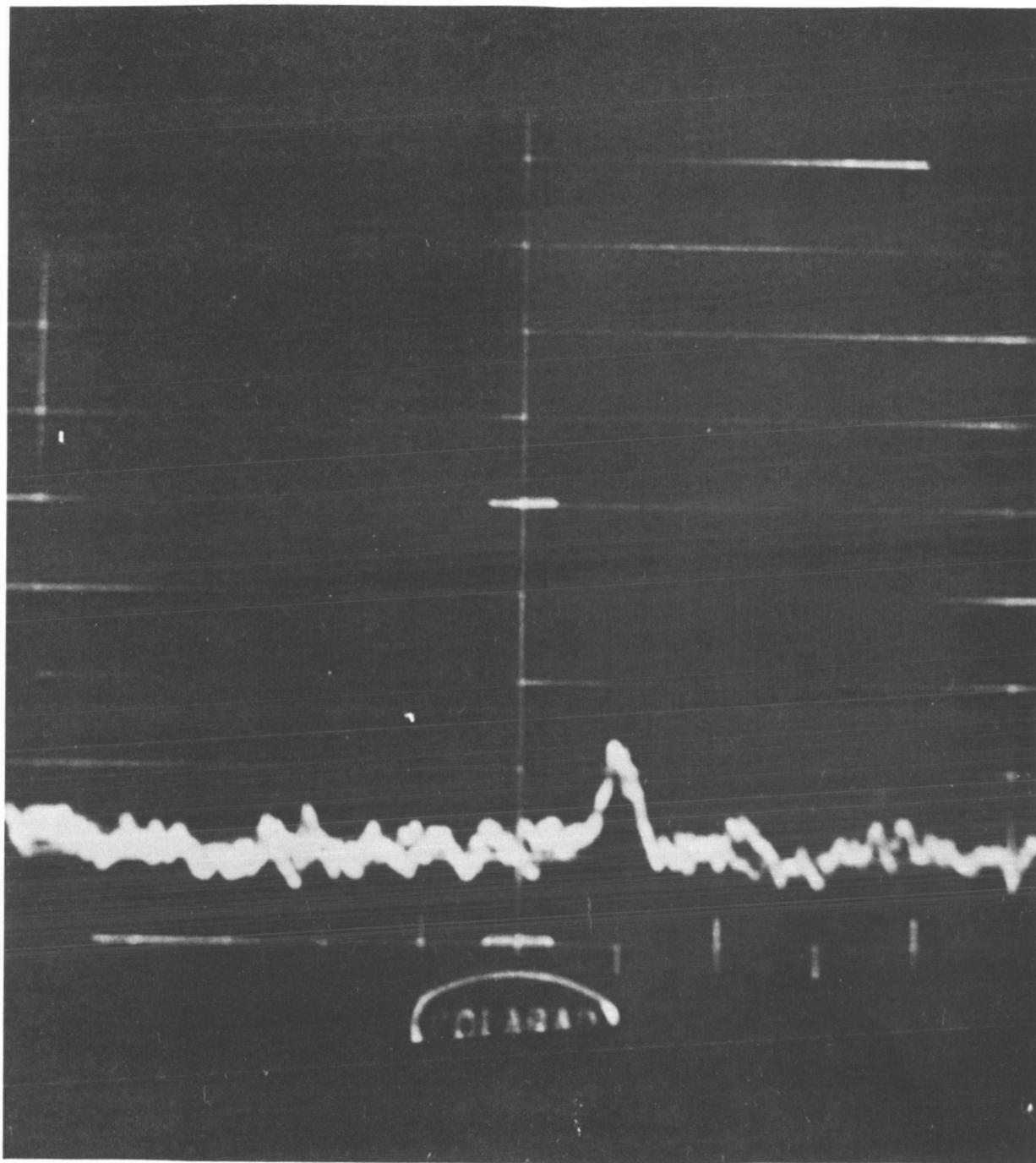


Figure 15b - Out-of-Phase Signal Strength

Table I

List and Short Description of Packaged
Equipment Used in the Ranging System

- PERKIN-ELMER 5300 Helium-Neon Gas Laser: a d-c excited source of polarized diffraction-limited radiation. Output is at 6328 \AA ; long radius resonator configuration
- PERKIN-ELMER 5300 Gas Laser Power Supply: d-c variable power supply
- RCA 7029 Photomultiplier: ten stage dormer-window type having S-17 response; wavelength of maximum response is $4900 \pm 500 \text{ \AA}$. This type makes use of cesium-antimony, semitransparent photocathode on a reflective substrate. The shape of the photocathode is rectangular on a concave spherical surface.
- JOHN FLUKE 412-A High Voltage Supply: d-c variable power supply
- GAERTNER Optical Bench: a heavy Meehanite casting normalized before final machining to assure permanent straightness of the guides. It is 166 by 11 by 15 centimeters and weighs 150 lbs. The scale for determining the position of the carriages is 160 cm. long and is attached to the bench parallel with the guides. It is engine divided in millimeters with every centimeter numbered.
- TEKTRONIX L-20 Spectrum Analyzer: plug-in unit.
-

1. Determination of the Laser Difference Frequency Stability

Before any meaningful data could be taken, it was necessary to establish the frequency stability of the laser difference frequency. Figure 16 shows the experimental arrangement used to accomplish this. The laser beat frequency, approximately 170 MHz, was mixed with a 162 MHz signal from a Hewlett-Packard signal generator. The resultant signal was then fed into a spectrum analyzer tuned to 8 MHz and the difference frequency was monitored. The laser difference frequency was beat down to a lower frequency in order to more accurately detect frequency drifts.

The resultant 8 MHz signal was centered on the spectrum analyzer and the drift was recorded every hour for five hours. Data from these measurements is tabulated in Table II. Figure 17 shows the actual drift observed on the spectrum analyzer after one hour of frequency monitoring.

Table II

Tabulation of Laser Beat-Note Frequency Drift—Long term drift.

Time	Drift on Screen in Centimeters	Drift/hr.
-	centered at 8 MHz on spectrum analyzer	-
1 hr.	3 cm.	39.99 kHz/hr.
2 hr.	4 cm.	53.32 kHz/hr.
3 hr.	2 cm.	26.66 kHz/hr.
4 hr.	3.6 cm.	47.98 kHz/hr.
5 hr.	2.5 cm.	39.99 kHz/hr.

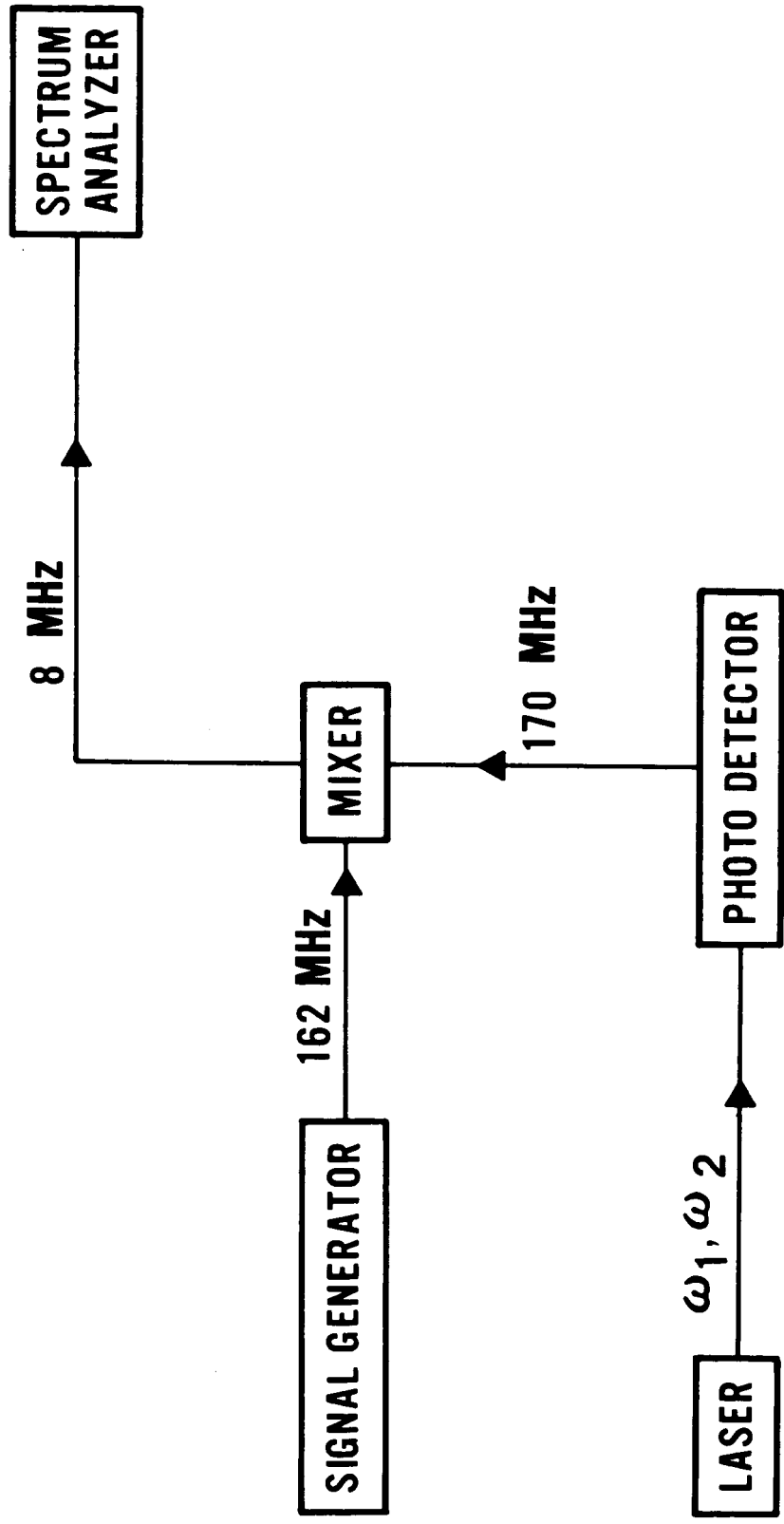


Figure 16 - Circuit to Monitor Beat-Note Signal Strength

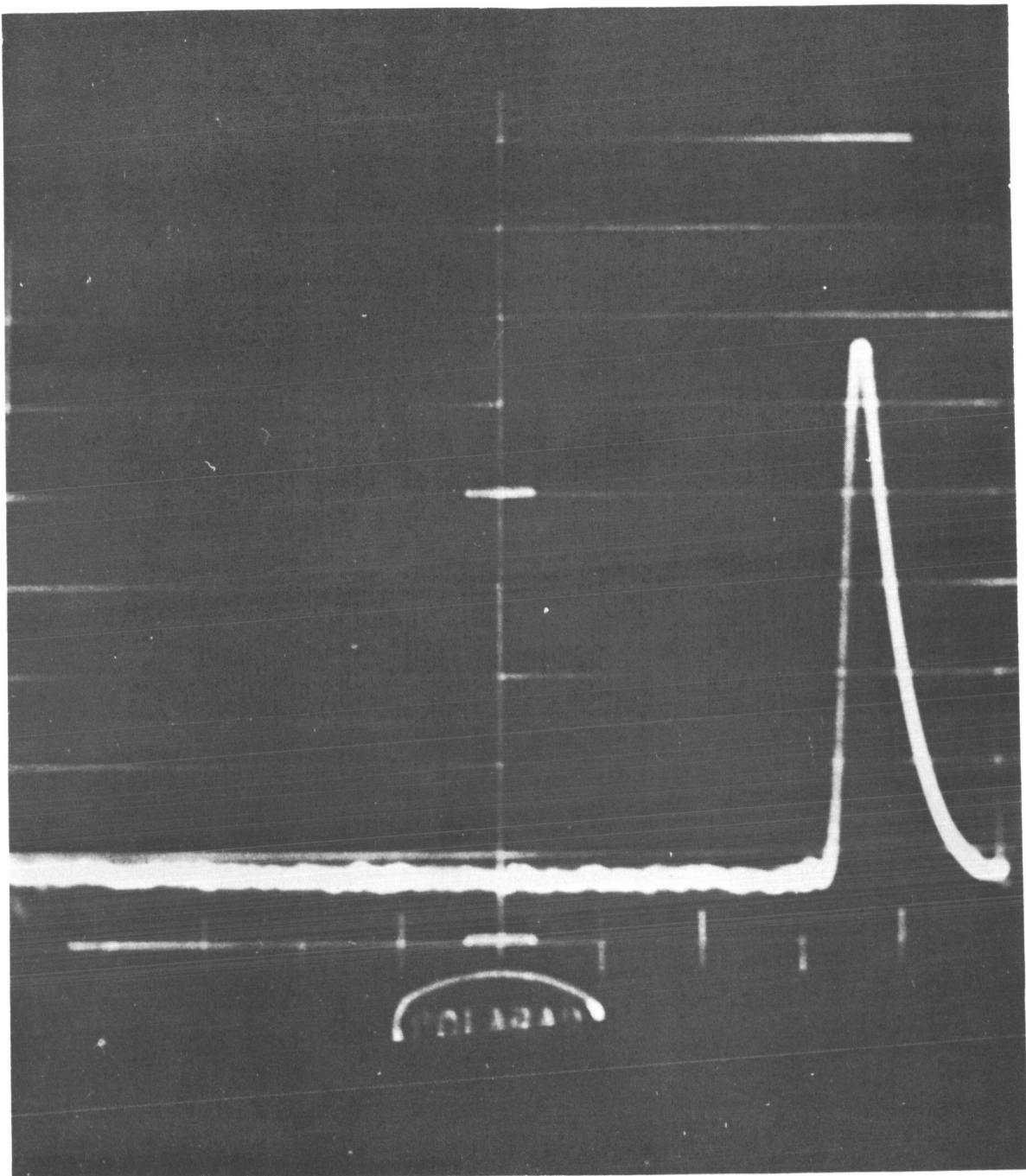


Figure 17 - Photograph of Frequency Drift of
Laser Beat-Note after One Hour

The difference frequency was observed to drift approximately 40.3 kHz/hour. This drift was reduced manually by adjusting the resonator configuration whenever a large signal drift was detected on the spectrum analyzer. This measurement of long-term stability implies stability of the signal generator and the spectrum analyzer. However, neither the signal generator nor the spectrum analyzer has a crystal-controlled oscillator. Therefore, a frequency drift in the signal generator and/or the spectrum analyzer could offset the laser instability; as a consequence, the laser beat-note signal could appear more or less stable than it actually is.

It was also considered necessary to run a data check on the short term stability of the beat-note. The laser difference frequency was fed into a crystal-controlled frequency counter and monitored. The recorded data, taken in ten second intervals for a period of ten minutes, is tabulated in Table III. This check on the short term stability of the beat note showed a random frequency fluctuation of over 87 kHz in the ten minute period.

This short-term stability measurement also indicates the measured long-term stability is not as accurate as the data implies. As stated before, this inconsistency could be due to two factors: instability in the signal generator 162 MHz signal and instability in the tuning circuit of the spectrum analyzer -- both of which could offset the beat note instability.

Table III

Beat-Note Frequency of the Laser Monitored on a Frequency Counter

10 Second Time Intervals	Beat-Note Frequency (Hz/s)	10 Second Time Intervals	Beat-Note Frequency (Hz/s)
1	170, 702, 701.0	31	170, 687, 992.5
2	170, 678, 361.3	32	170, 690, 644.5
3	170, 679, 972.8	33	170, 694, 061.4
4	170, 685, 198.3	34	170, 696, 342.5
5	170, 670, 387.3	35	170, 696, 452.4
6	170, 663, 626.8	36	170, 696, 005.0
7	170, 660, 316.8	37	170, 693, 830.5
8	170, 687, 143.8	38	170, 687, 744.7
9	170, 687, 572.2	39	170, 682, 835.6
10	170, 687, 946.7	40	170, 678, 704.3
11	170, 689, 667.6	41	170, 675, 431.0
12	170, 692, 447.4	42	170, 679, 247.2
13	170, 695, 255.9	43	170, 685, 830.0
14	170, 693, 268.9	44	170, 690, 021.6
15	170, 693, 133.4	45	170, 700, 651.8
16	170, 689, 086.5	46	170, 705, 748.2
17	170, 684, 536.4	47	170, 707, 806.1
18	170, 681, 081.4	48	170, 708, 655.8
19	170, 677, 133.6	49	170, 624, 245.5
20	170, 677, 594.6	50	170, 657, 201.2
21	170, 681, 930.4	51	170, 646, 251.5
22	170, 686, 756.5	52	170, 624, 685.2
23	170, 689, 982.3	53	170, 624, 803.9
24	170, 693, 654.2	54	170, 625, 731.5
25	170, 699, 179.7	55	170, 626, 990.3
26	170, 704, 281.2	56	170, 630, 217.6
27	170, 705, 126.2	57	170, 632, 102.6
28	170, 706, 557.3	58	170, 642, 041.4
29	170, 708, 668.7	59	170, 647, 194.0
30	170, 712, 077.3	60	170, 655, 475.8

2. Determination of Null Points and Data Reduction

Experimental verification of the predicted results from Equation (13) required the accurate determination of points of minimum intensity; it was also necessary to correlate the distance between null points with the wavelength of the beat note frequency.

The I_{RMS} signal from the interferometer arms was displayed on the spectrum analyzer, as mirror M_1 of the Michelson interferometer was moved down the optical bench. By this method, points of minimum I_{RMS} signal or null points were recorded.

Twenty readings were taken at each of the four null positions; the data at each null is tabulated in Table IV. As stated previously, the vernier scale on the optical bench and movable mount made it possible to read position accurately to a tenth of a millimeter. The frequency distribution of the readings at each null are given graphically in Figures 18-21. A statistical analysis of the accuracy to which each null can be read is given in Tables V-VIII.

Nulls A and B were measured on the same optical bench. Therefore the difference in length between these two nulls should correspond to a half-wavelength of the laser beat frequency since the path length of the light is doubled on reflection. The beat frequency is averaged from the short-term stability measurements to 170, 671, 766 Hz/s; from the relationship $c = \lambda f$ the wavelength associated with this frequency is calculated to be 1757.76 millimeters.

Theory thus predicts the difference between nulls to be $\lambda/2 = 878.9$ mm. The measured difference on the optical bench between nulls A and

Table IV
Data Giving Four Null Positions*

Null A (cm)	Null B (cm)	Null C (cm)	Null D (cm)
11.76	99.61	36.20	124.60
11.80	99.70	36.10	124.73
11.68	99.74	36.15	124.65
11.75	99.73	36.09	124.68
11.78	99.70	36.25	124.69
11.73	99.74	36.11	124.69
11.78	99.83	36.17	124.63
11.80	99.79	36.15	124.69
11.68	99.70	36.08	124.69
11.74	99.64	36.19	124.64
11.74	99.64	36.13	124.73
11.71	99.74	36.20	124.64
11.70	99.64	36.23	124.61
11.75	99.82	36.15	124.60
11.72	99.75	36.13	124.65
11.70	99.84	36.19	124.70
11.78	99.75	36.19	124.69
11.78	99.71	36.13	124.66
11.69	99.75	36.23	124.69
11.76	99.72	36.21	124.64

*Nulls C and D give an absolute path length reading of ten wavelengths plus the actual reading recorded.

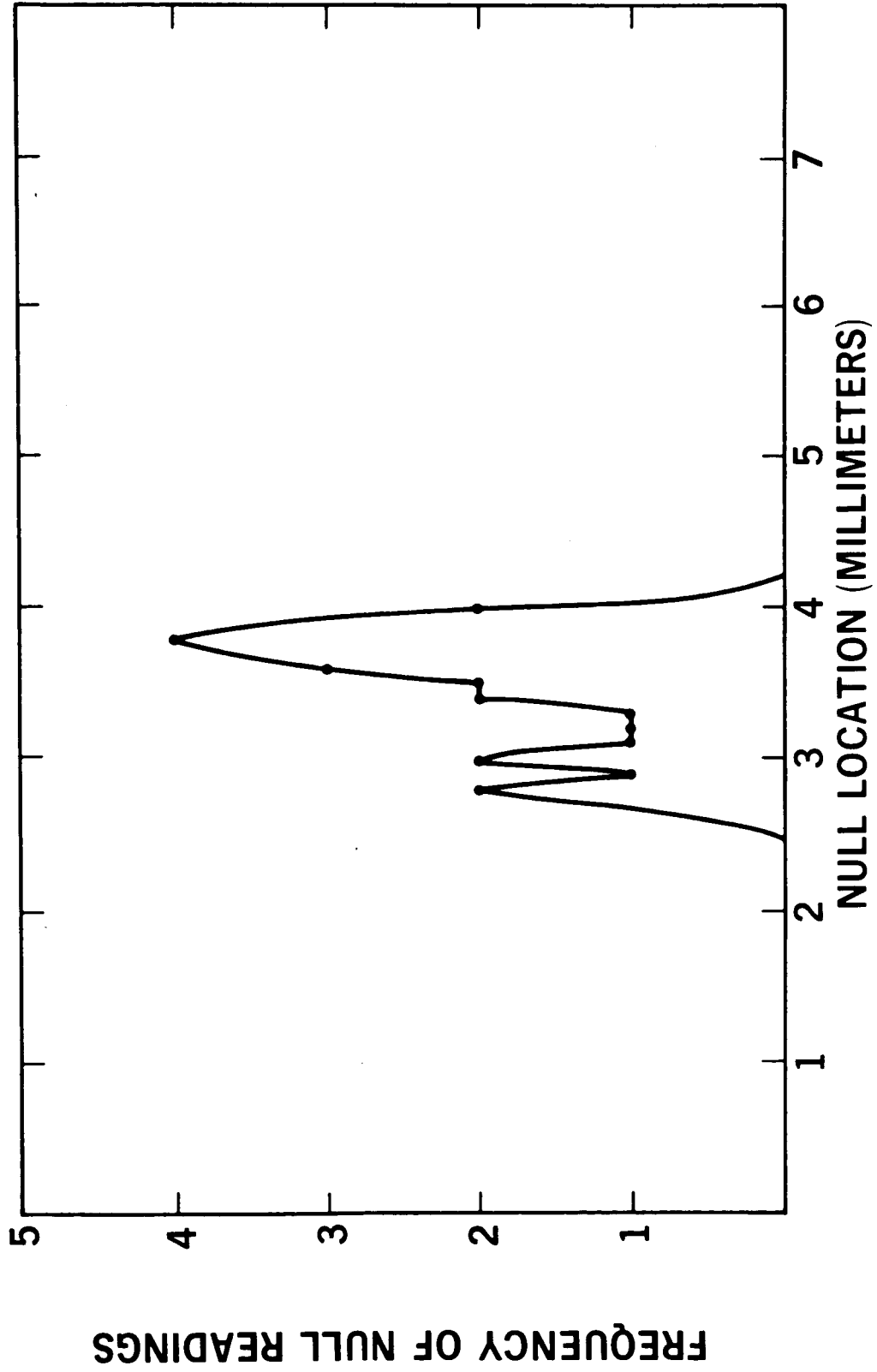


Figure 18 - Distribution of Readings for Null A

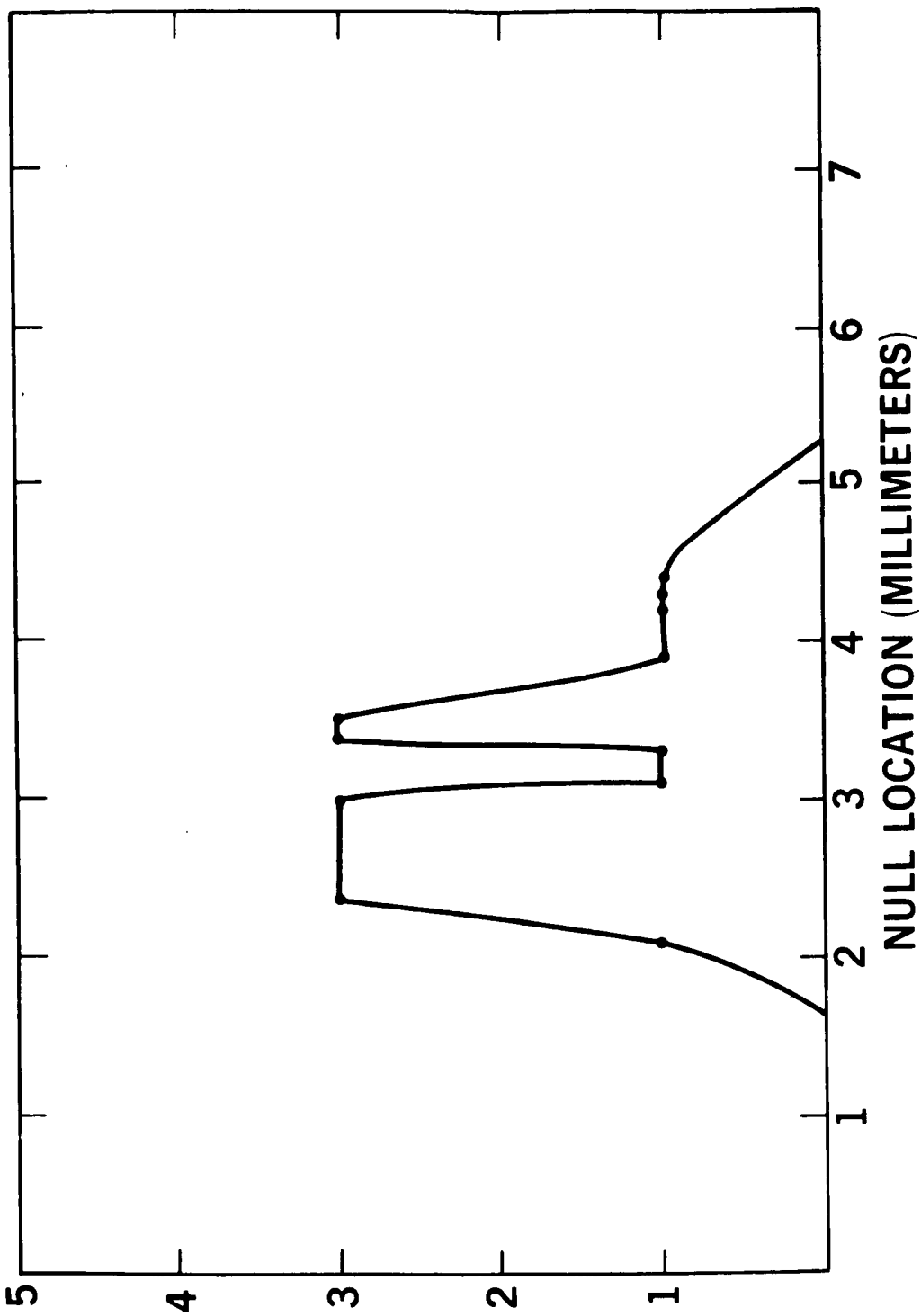
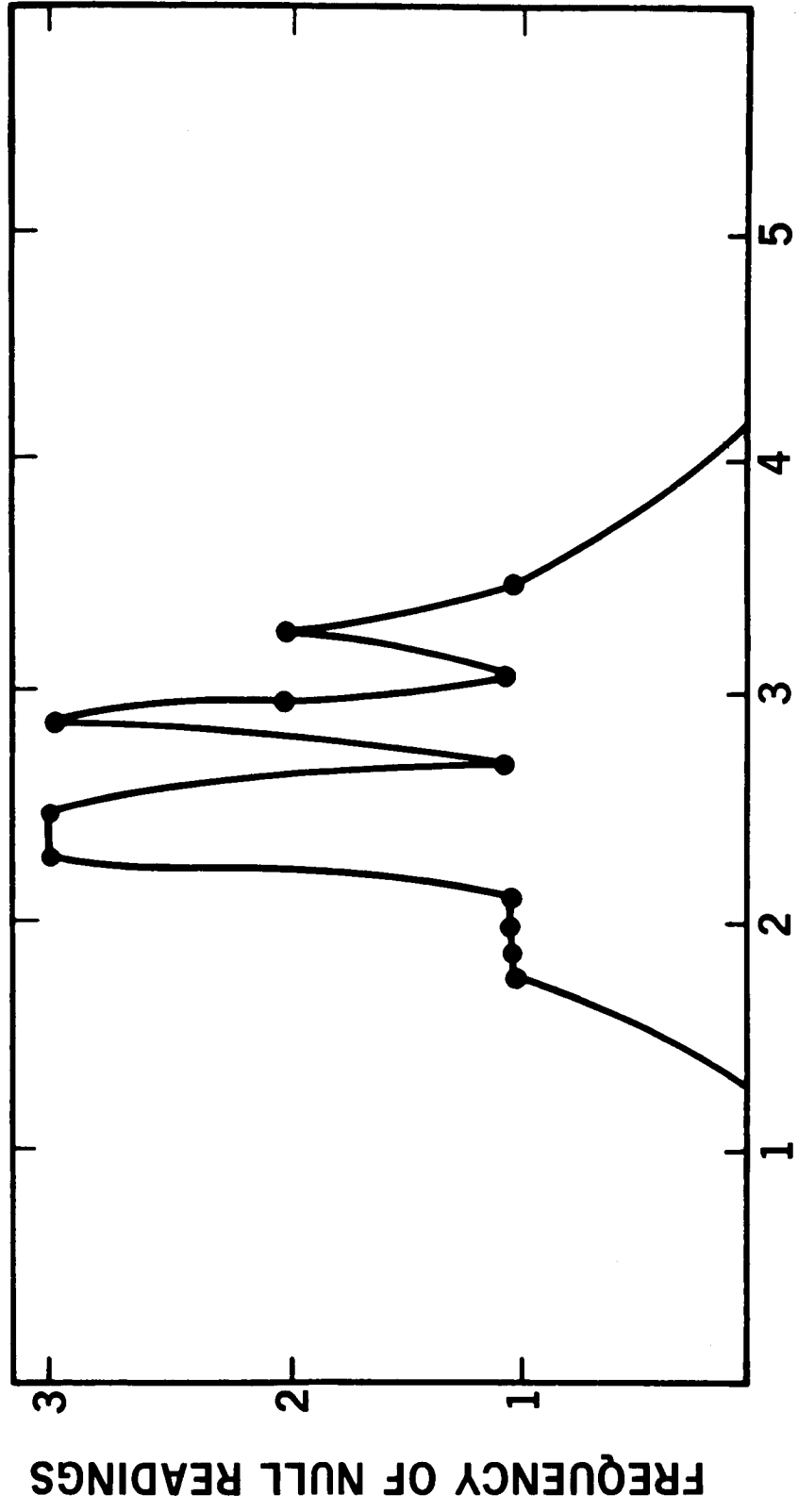


Figure 19 - Distribution of Readings for Null B



NULL LOCATION (MILLIMETER)
Figure 20 - Distribution of Readings for Null C

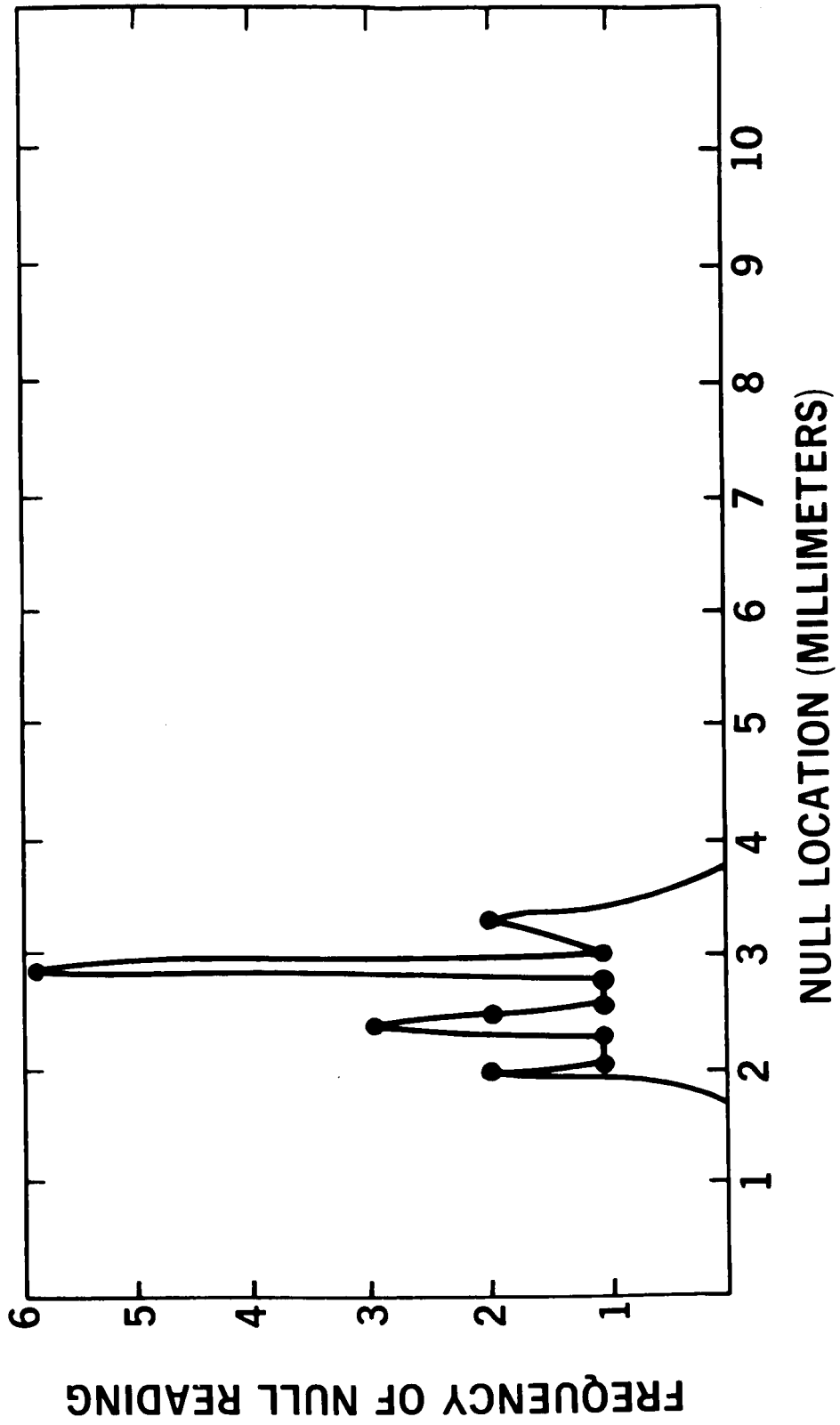


Figure 21 - Distribution of Readings for Null D

Table V
Statistical Analysis of Null A

Null Readings (cm)	Deviation, ρ	ρ^2
11.76	+ .02	4×10^{-4}
11.80	+ .06	36×10^{-4}
11.68	- .06	36×10^{-4}
11.75	+ .01	1×10^{-4}
11.78	+ .04	16×10^{-4}
11.73	- .01	1×10^{-4}
11.78	+ .04	16×10^{-4}
11.80	+ .06	36×10^{-4}
11.68	- .06	36×10^{-4}
11.74	0.00	-
11.74	0.00	-
11.71	- .03	9×10^{-4}
11.70	- .04	16×10^{-4}
11.75	+ .01	1×10^{-4}
11.72	- .02	4×10^{-4}
11.70	- .04	16×10^{-4}
11.75	+ .01	1×10^{-4}
11.72	- .02	4×10^{-4}
11.70	- .04	16×10^{-4}
11.78	+ .04	16×10^{-4}
11.78	.04	16×10^{-4}
11.69	- .05	25×10^{-4}
11.76	+ .02	4×10^{-4}

$$\sum_{i=1}^{20} n = 234.83$$

$$\sum_{i=1}^{20} \rho^2 = 3.10 \times 10^{-2}$$

$$\bar{n} = \frac{\sum n}{20} = 11.74$$

$$\sigma = \sqrt{\sum \rho^2 / n} = \sqrt{15.5 \times 10^{-4}}$$

$$\therefore \sigma = 3.93 \times 10^{-2}$$

Null A: $11.74 \pm .04$ cm or $117.4 \pm .4$ mm

Table VI
Statistical Analysis of Null B

Null Readings (cm)	Deviation, ρ	ρ^2
99.61	- .12	144×10^{-4}
99.70	- .03	9×10^{-4}
99.74	+ .01	1×10^{-4}
99.73	.00	-
99.70	- .03	9×10^{-4}
99.74	+ .01	1×10^{-4}
99.83	+ .10	100×10^{-4}
99.79	+ .06	36×10^{-4}
99.70	- .03	9×10^{-4}
99.64	- .09	81×10^{-4}
99.64	- .09	81×10^{-4}
99.74	+ .01	1×10^{-4}
99.64	- .09	81×10^{-4}
99.82	+ .09	81×10^{-4}
99.75	+ .02	4×10^{-4}
99.71	- .02	4×10^{-4}
99.75	+ .02	4×10^{-4}
99.72	- .01	1×10^{-4}
99.84	+ .11	121×10^{-4}
99.75	+ .02	4×10^{-4}

$$\sum_{i=1}^{20} n = 1994.54$$

$$\sum_{i=1}^{20} \rho^2 = 7.72 \times 10^{-2}$$

$$\bar{n} = \frac{\sum n}{20} = 99.73$$

$$\sigma = \sqrt{\sum \rho^2 / n} = \sqrt{35.6 \times 10^{-4}}$$

$$\sigma = 5.96 \times 10^{-2}$$

Null B: $99.73 \pm .06$ cm or $997.3 \pm .6$ mm

Table VII
Statistical Analysis of Null C

Null Readings (cm)	Deviation, ρ	ρ^2
36.20	+ .04	16×10^{-4}
36.10	- .06	36×10^{-4}
36.15	- .01	1×10^{-4}
36.09	- .07	49×10^{-4}
36.25	+ .09	81×10^{-4}
36.11	- .05	25×10^{-4}
36.17	+ .01	1×10^{-4}
36.15	- .01	1×10^{-4}
36.08	- .08	64×10^{-4}
36.19	+ .03	9×10^{-4}
36.13	- .03	9×10^{-4}
36.20	+ .04	16×10^{-4}
36.23	+ .07	49×10^{-4}
36.15	- .01	1×10^{-4}
36.13	- .03	9×10^{-4}
36.19	+ .03	9×10^{-4}
36.19	+ .03	9×10^{-4}
36.13	- .03	9×10^{-4}
36.23	+ .07	49×10^{-4}
36.21	+ .05	25×10^{-4}

$$\sum_{i=1}^{20} n = 723.28$$

$$\sum_{i=1}^{20} \rho^2 = 4.68 \times 10^{-2}$$

$$\bar{n} = \frac{\sum n}{20} = 36.16$$

$$\sigma = \sqrt{\rho^2/n} = \sqrt{23.4 \times 10^{-4}}$$

$$\sigma = 4.84 \times 10^{-2}$$

Null C: $36.16 \pm .05$ cm or $361.6 \pm .5$ mm

Table VIII
Statistical Analysis of Null D

Null Readings (cm)	Deviation, ρ	ρ^2
124.60	+ .07	49×10^{-4}
124.73	+ .06	36×10^{-4}
124.65	- .02	4×10^{-4}
124.68	+ .01	1×10^{-4}
124.69	+ .02	4×10^{-4}
124.69	+ .02	4×10^{-4}
124.63	- .04	16×10^{-4}
124.69	+ .02	4×10^{-4}
124.69	+ .02	4×10^{-4}
124.64	- .03	9×10^{-4}
124.73	+ .06	36×10^{-4}
124.64	- .03	9×10^{-4}
124.61	- .06	36×10^{-4}
124.60	- .07	49×10^{-4}
124.65	- .02	4×10^{-4}
124.70	+ .03	9×10^{-4}
124.69	+ .02	4×10^{-4}
124.66	- .01	1×10^{-4}
124.69	+ .02	4×10^{-4}
124.64	- .03	9×10^{-4}

$$\sum_{i=1}^{20} n = 2493.30$$

$$\sum_{i=1}^{20} \rho^2 = 2.92 \times 10^{-2}$$

$$\bar{n} = \frac{\sum n}{20} = 124.67$$

$$\sigma = \sqrt{\rho^2/n} = \sqrt{14.6 \times 10^{-4}}$$

$$\sigma = 3.82 \times 10^{-2}$$

Null D: $124.67 \pm .04$ cm or $1246.7 \pm .4$ mm

B is: 879.9 ± 1.0 mm. The path length difference between points of minimum intensity is therefore accurate to within the calculated limits of error.

Nulls C and D, measured on another optical bench were ten wavelengths from the beam splitter plus the recorded readings. The path difference between these two nulls should also correspond to a half-wavelength of the beat-note frequency. However in this case the path difference is measured to be $885.1 \pm .9$ mm. This gives a percentage error of .49 percent between the predicted half-wavelength value and the actual length measured.

3. Results

A careful examination of the recorded data verifies that Equation (13) does predict a precision-ranging system. Variations in the I_{RMS} displayed on the signal analyzer indicated variations in the path length of the two interferometer arms. Minimum signal strength on the spectrum analyzer corresponded to null points (that is, light beams from the interferometer arms are 180° out of phase). These null points could be repeatably located to about $\pm .6$ mm. of their average location.

The first cause of error in accurately determining the precise location of the null points is the laser instability. Equation (19) allows one to calculate the amount of error introduced in measuring L due to the instability of the difference frequency.

However as seen in the theoretical analysis, there is also another source of error. Shot noise due to random fluctuation in the ω_1 , ω_2 ,

and $\omega_1 + \omega_2$ components in the photomultiplier causes inaccuracy in the precise location of null points. If the two arms of the interferometer are of equal intensity, the I_{RMS} signal becomes lost in the noise on the spectrum analyzer at a null point. The accuracy of the system is not increased if the intensity in one arm of the interferometer is decreased. The continual "jitter" from the shot noise which rides on the 170 MHz signal makes accurate measurements by the naked eye difficult.

Equation (13) shows I_{RMS} as a function of the cosine of the length measure. It predicts the correlation of the distance travelled by the movable arm of the interferometer with the I_{RMS} measured. This is experimentally verified by the accurate measurement of the distance between nulls. The difference in length between nulls A and B corresponds to a half-wavelength of the laser beat frequency.

The .5 percent difference between the theoretical path length, the half-wavelength of the laser beat note, and the actual path length from Null C to Null D is most probably a result of the laser instability. For a continuous frequency drift of the laser self-beat would result in a shift in the corresponding half-wavelength. A ten kHz variation in the signal at a ten meter range results in an uncertainty in length of approximately $\pm .5$ millimeters.

C. Alternate High Accuracy Ranging System

1. Method of Frequency Stabilization of the Laser

The proposed ranging system would have a wider application area if the accuracy of the measurements could be increased. As previously

discussed, the two sources of error are shot noise and frequency instability.

No significant reduction of the shot noise level was achieved by narrowing the bandwidth of the system or by reducing the dark current. Frequency components ω_1 , ω_2 , and $\omega_1 + \omega_2$ which result in the d-c level dominated the shot noise. At present, attempts to minimize these components have been unsuccessful.

However, the main source of error, beat-frequency instability, can be minimized by the development of a stabilized laser. In the visible and near infra-red gas laser, the atomic resonance is much broader than the cavity resonance. Consequently, the laser frequency stability depends almost entirely on the stability of the cavity resonance.

Frequency variations due to fluctuations in the refractive index of the inverted population and electron density are not usually observed unless the discharge is electrically "noisy." At line center, fluctuations in inverted population have a negligible effect on the cavity resonance. Much more serious, since they are difficult to eliminate, are mechanical vibrations and resonances of the cavity generated by airborne sound waves or building vibrations. Also, temperature variations cause the length of the laser cavity to change slightly. The magnitude of the problem is evident from the fact that a 100 micron change in mirror spacing in a 60 centimeter cavity produces a frequency shift of 41 kHz in the laser beat note.

Feedback stabilized lasers incorporate basically the same elements utilized in stabilized oscillators operating at lower frequencies. Common

to all such systems is a null-type frequency discriminator which converts deviations in oscillator frequency into a time-varying error signal. The amplitude and polarity of the error signal reflects the magnitude and sign of the frequency deviation. After suitable amplification, the signal is used to drive the oscillator frequency towards the discriminator null frequency. The overall response of the system to short-term disturbances depends on the servo-loop bandwidth and the discriminator sensitivity. The long-term stability of the system is no better than the stability of the discriminator null frequency.¹²

In this case, the self-beat of the gas laser is phase-locked to a frequency standard. The circuit to accomplish this, shown in Figures 22 and 23, was designed by Syracuse Research Corporation.³ The laser was an r-f pumped helium-neon laser operating at 6328 \AA .

The resonator used to produce the uniphase wave fronts was of the hemispherical configuration. As shown in Figure 24, this resonator consists of a spherical mirror and a plane mirror placed approximately at the center of curvature of the sphere. The end mirrors are of Schlieren grade fused silica coated for optimum performance at 6328 \AA . The flat mirror is coated to provide reflectivity greater than 99.7 percent; and the spherical mirror is coated for lower reflectivity on the order of 98 percent. It is from this mirror that the maximum intensity emanates. The resultant modes have a relatively large diameter at the spherical mirror and focus to a diffraction limited point at the plane mirror.

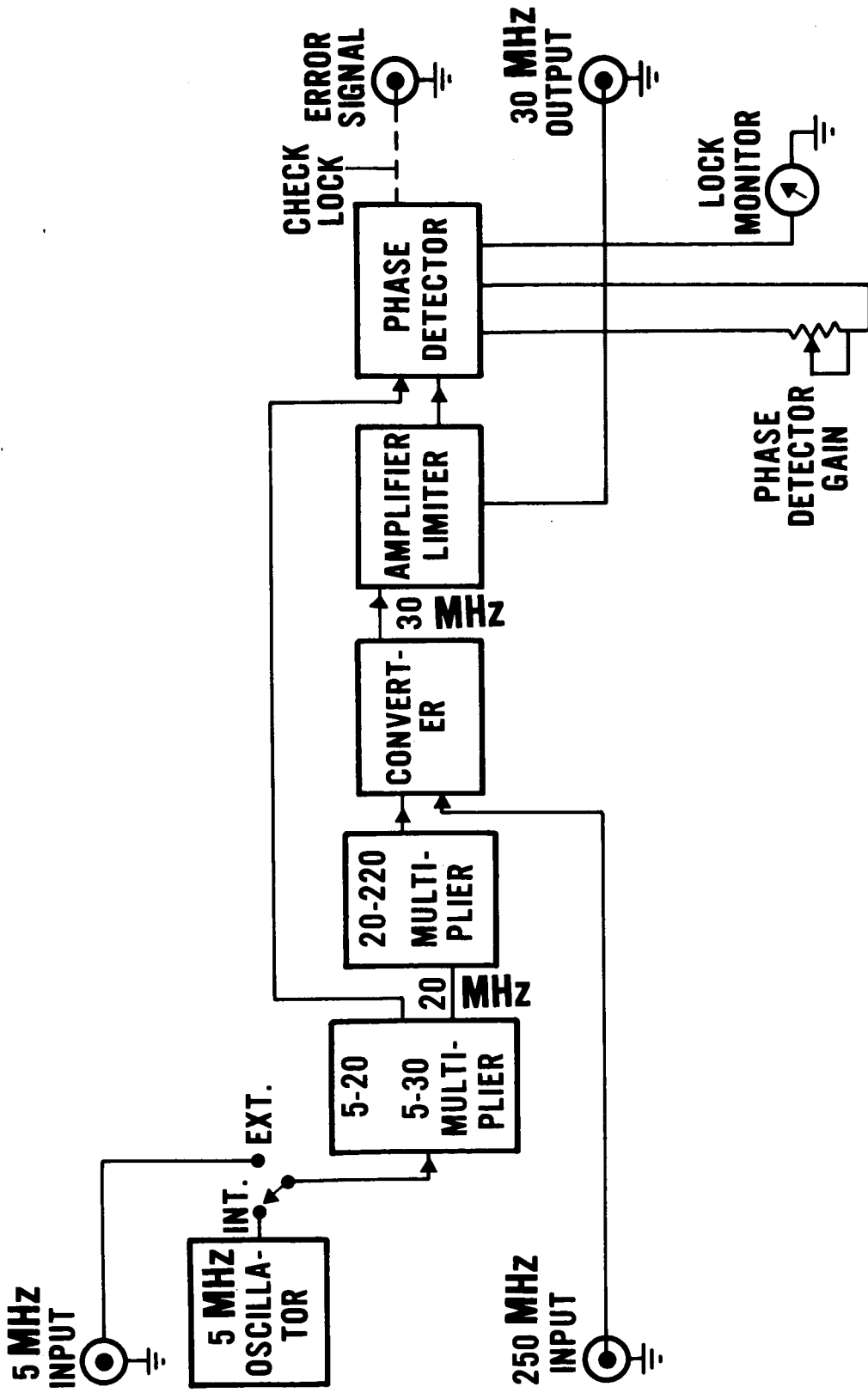


Figure 22 - Locking Circuit Used to Stabilize the Self-Beat of the Laser

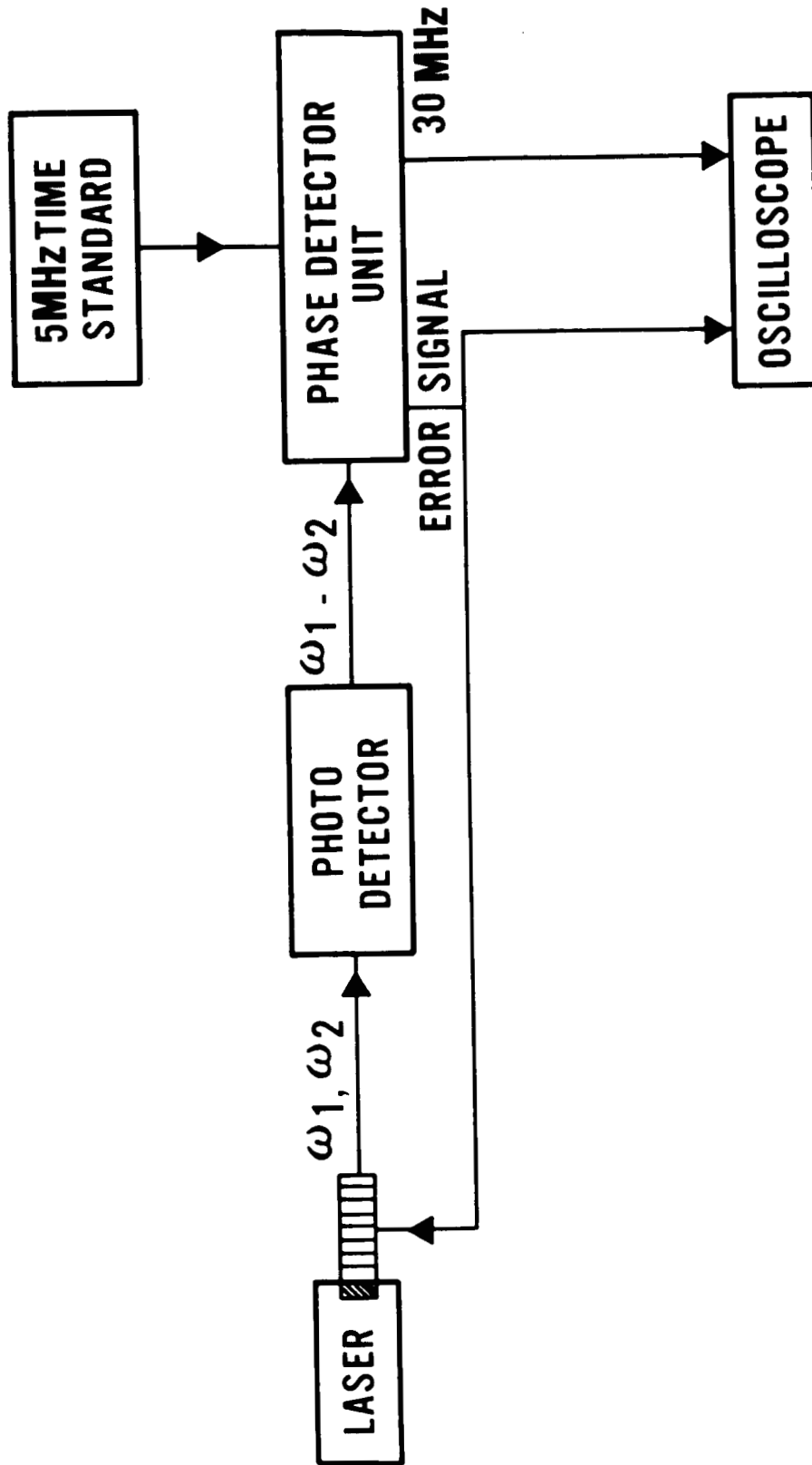
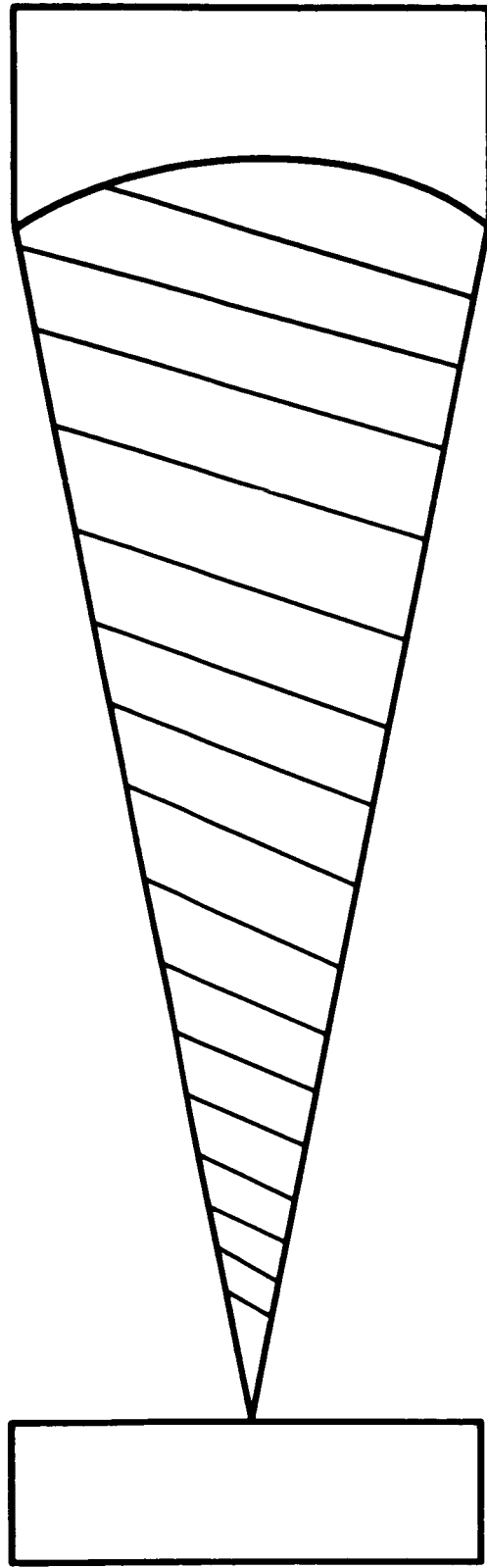


Figure 23 - Laser Stabilization Loop

PLANE MIRROR

SPHERICAL MIRROR



INDICATES INTRACAVITY RADIATION

Figure 24 - Hemispherical Resonator Configuration Giving Uniphase Wavefronts

The two advantages in using this configuration are the ability to choose the mode dimension by small variations in the separation of the mirrors, and the relative ease of adjustment of the mirrors with regard to parallelism. This adjustment is non-critical since angular misalignment of the flat mirror results in a smaller part of the spherical mirror forming a useful cavity. The laser will oscillate on a smaller part of the spherical mirror if diffraction losses permit.

The TEM_{00q} and TEM_{00q+1} modes were excited by using a 24 MHz crystal controlled transmitter. The end mirrors were adjusted for a difference frequency of 250 MHz/s. These two modes were received and mixed in an RCA photomultiplier tube; the beat frequency signal was then amplified and beat down to 30 MHz. This signal was referenced against a 30 MHz signal derived from a frequency time standard, stable to one part in 10^{10} . The resulting error signal was amplified and fed back to the laser. This method maintained a constant cavity length by applying an error signal to a stack of ceramic discs mounted on the plane mirror in the resonator cavity.

These discs were composed of lead titanate zirconate, a piezoelectric ceramic. The advantage in using this ceramic is its great stiffness; mechanical deflections in response to a driving signal are very small, but they are not easily constrained.⁴ The sensitivity of the ceramic transducer was such that the beat frequency could be changed 70 (Hz/s)/v at 8 kHz/s.

To measure the accuracy of the servo-lock loop an electronic counter was used to monitor the difference frequency. In this

way it was possible to lock the self-beat of the laser at 250 MHz \pm 1 Hz.

2. Determination of Null Points and Data Reduction

The ranging system seen in Figure 25 was the same as that previously described with the addition of the servo-loop to lock the difference frequency. The I_{RMS} signal from the interferometer arms was displayed on the spectrum analyzer. The location of two null points was established by monitoring the I_{RMS} on the spectrum analyzer as mirror M_1 of the Michelson interferometer was moved down the optical bench. By this method, points of minimum I_{RMS} signal or null points were recorded.

Thirty readings were taken at each of the two null positions; the data at each null is tabulated in Table IX. The frequency distribution of the readings at each null are given graphically in Figures 26 and 27. A statistical analysis of the accuracy to which each null can be read is given in Tables X and XI.

Because the light path is doubled on reflection from mirror M_1 the difference in length between the two nulls should correspond to a half-wavelength of the beat frequency. The wavelength associated with the beat frequency of 250 MHz is calculated to be 1199.0 millimeters. Theory predicts the difference between nulls to be $\lambda/2 = 599.5$ millimeters. The measured difference on the optical bench between nulls A' and B' is $600.0 \pm .6$ millimeters. Thus the linear path difference between points of minimum intensity is accurate to within the calculated limits of error.

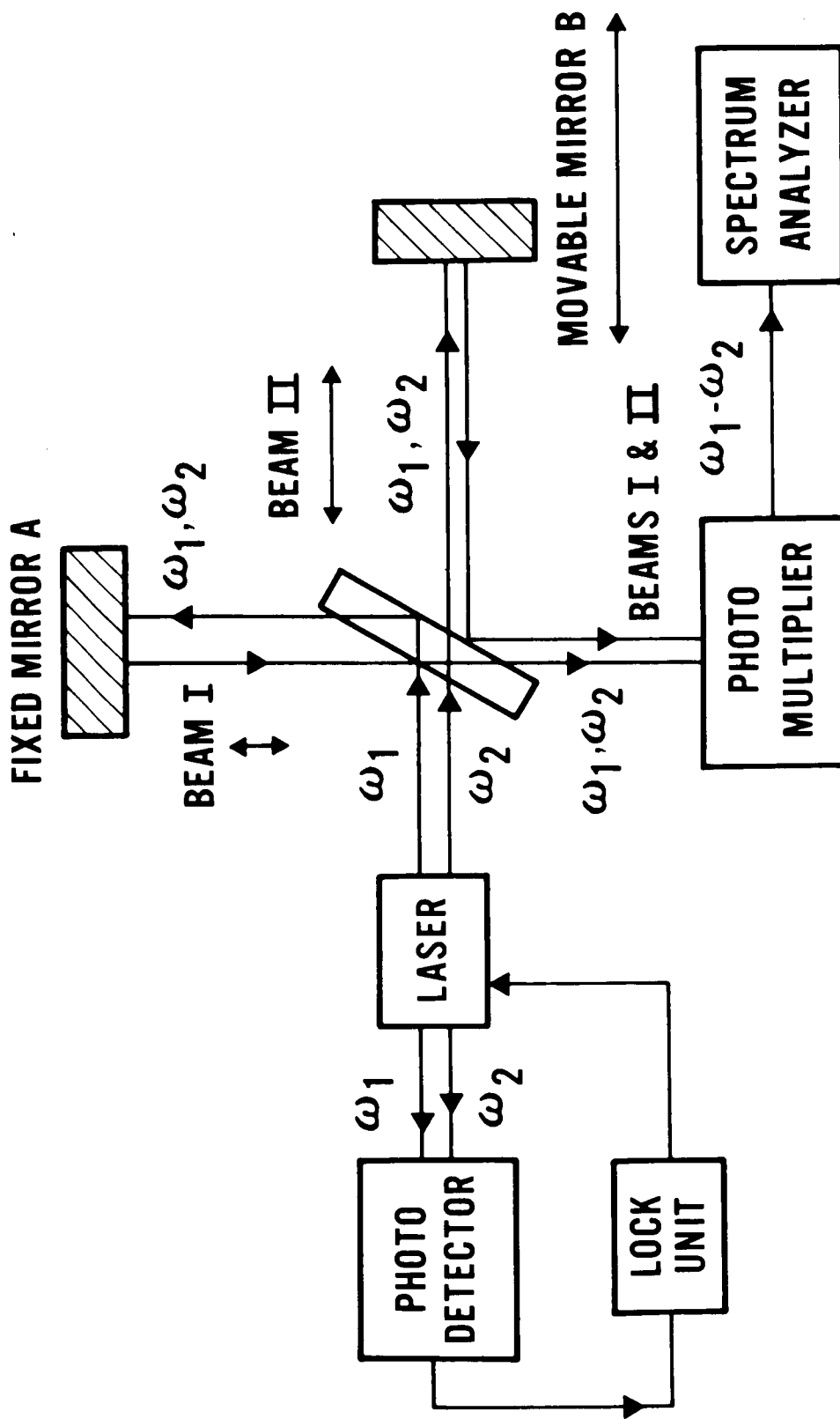


Figure 25 - Experimental Ranging System with Stabilized Laser

Table IX

Data Giving Null Positions [Ranging system utilizing stabilized laser].

Null A'	Null B'
139.30	199.25
139.28	199.27
139.21	199.31
139.29	199.26
139.30	199.29
139.22	199.21
139.28	199.30
139.24	199.27
139.29	199.28
139.25	199.31
139.27	199.25
139.32	199.24
139.31	199.27
139.28	199.29
139.22	199.22
139.27	199.30
139.25	199.31
139.29	199.28
139.29	199.23
139.28	199.25
139.25	199.21
139.28	199.28
139.31	199.27
139.27	199.28
139.26	199.25
139.25	199.27
139.30	199.24
139.27	199.29
139.28	199.27
139.29	199.24

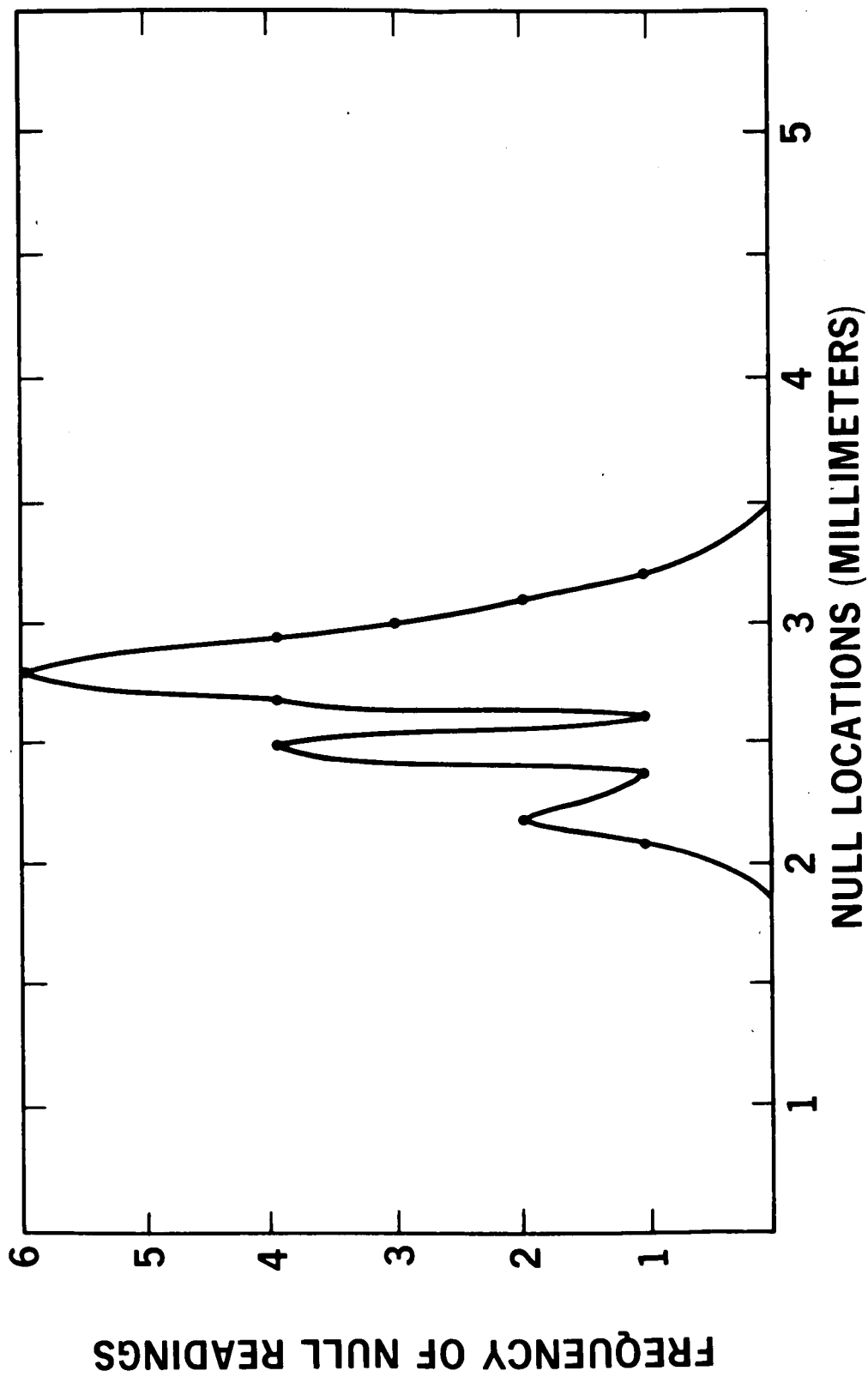


Figure 26 - Distribution of Readings for Null A'

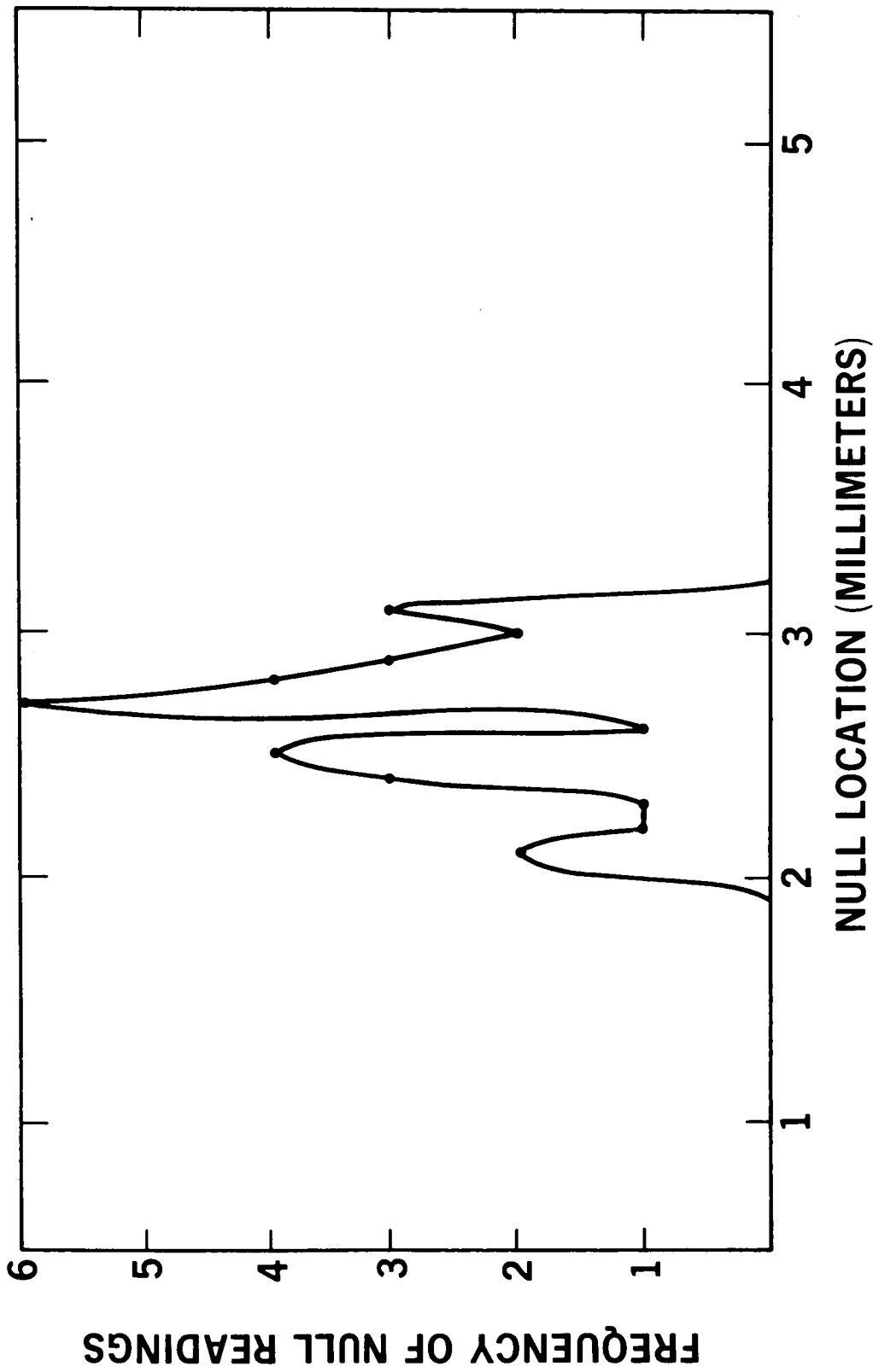


Figure 27 - Distribution of Readings for Null B'

Table X
Statistical Analysis of Null A'

Null Readings (cm)	Deviation, ρ	ρ^2
139.30	+ .03	9×10^{-4}
139.28	+ .01	1×10^{-4}
139.21	- .06	36×10^{-4}
139.29	+ .02	4×10^{-4}
139.30	+ .03	9×10^{-4}
139.28	+ .01	1×10^{-4}
139.22	- .05	25×10^{-4}
139.24	- .03	9×10^{-4}
139.29	+ .02	4×10^{-4}
139.25	- .02	4×10^{-4}
139.27	.00	-
139.32	+ .05	25×10^{-4}
139.31	+ .04	16×10^{-4}
139.28	+ .01	1×10^{-4}
139.22	- .05	25×10^{-4}
139.27	.00	-
139.25	- .02	4×10^{-4}
139.29	+ .02	4×10^{-4}
139.29	+ .02	4×10^{-4}
139.28	+ .01	1×10^{-4}
139.25	- .02	4×10^{-4}
139.28	+ .01	1×10^{-4}
139.31	+ .04	16×10^{-4}
139.27	.00	-
139.26	- .01	1×10^{-4}
139.25	- .02	4×10^{-4}
139.30	+ .03	9×10^{-4}
139.27	.00	-
139.28	+ .01	1×10^{-4}
139.29	+ .02	4×10^{-4}

$$\sum_{i=1}^{30} n = 4178.20$$

$$\bar{n} = \frac{\sum n}{30} = 139.27$$

$$\sum_{i=1}^{30} \rho^2 = 2.12 \times 10^{-2}$$

$$\sigma = \sqrt{\sum \rho^2 / n} = \sqrt{7.07 \times 10^{-4}}$$

$$\therefore \sigma = 2.66 \times 10^{-2}$$

Null A: $139.27 \pm .03$ cm or $1392.7 \pm .3$ mm

Table XI
Statistical Analysis of Null B'

Null Readings (cm)	Deviation, ρ	ρ^2
199.25	- .02	4×10^{-4}
199.27	-	-
199.31	+ .04	16×10^{-4}
199.26	- .01	1×10^{-4}
199.29	+ .02	4×10^{-4}
199.21	- .05	25×10^{-4}
199.30	+ .03	9×10^{-4}
199.27	-	-
199.28	+ .01	1×10^{-4}
199.31	+ .04	16×10^{-4}
199.25	- .02	4×10^{-4}
199.24	- .03	9×10^{-4}
199.27	-	-
199.29	+ .02	4×10^{-4}
199.22	- .05	25×10^{-4}
199.30	+ .03	9×10^{-4}
199.31	+ .04	16×10^{-4}
199.28	+ .01	1×10^{-4}
199.23	- .04	16×10^{-4}
199.25	- .02	4×10^{-4}
199.21	- .06	36×10^{-4}
199.28	+ .01	1×10^{-4}
199.27	-	-
199.28	+ .01	1×10^{-4}
199.25	- .02	4×10^{-4}
199.27	-	-
199.24	- .03	9×10^{-4}
199.29	+ .02	4×10^{-4}
199.27	-	-
199.24	- .03	9×10^{-4}

$$\sum_{i=1}^{30} n = 5977.99$$

$$\sum_{i=1}^{30} \rho^2 = 2.28 \times 10^{-2}$$

$$\bar{n} = \frac{\sum n}{30} = 199.27$$

$$\sigma = \sqrt{\sum \rho^2 / n} = \sqrt{7.60 \times 10^{-4}}$$

$$\sigma = 2.76 \times 10^{-2}$$

Null B: $199.27 \pm .03$ cm or $1992.7 \pm .3$ mm

3. Results

Examination of the data shows an increased accuracy in linear measurements when a stabilized laser is utilized to eliminate one cause of error in determining the precise location of null points. With the laser stabilized to one part in 10^8 , null points could be located to within ± 0.3 millimeters of their average location. This remaining error is attributed to shot noise due to random fluctuations in the ω_1 , ω_2 , and $\omega_1 + \omega_2$ components in the photomultiplier. The linear path difference between points of minimum intensity is accurate to within the calculated limits of error; this difference in length between nulls A' and B' corresponds to a half-wavelength of the laser beat-frequency.

This data thus provides an experimental verification of the results predicted by Equation (13). It reconfirms that I_{RMS} is a function of the cosine of the length measured and shows the correlation of the distance travelled by the movable arm of the interferometer with the I_{RMS} measured.

PART IV

CONCLUSION

This report has analyzed the merits of an interferometric type ranging system which utilizes a continuous-wave laser. The theoretical analysis establishes the relation between phase information from the photomixing of two monochromatic light beams and the variation in path lengths of these two signals.

The experimental ranging system devised utilizes the difference frequency between adjacent TEM longitudinal modes of c-w laser to make accurate distance measurements. The accuracy of this ranging device is limited by two factors -- the system's noise level, due primarily to shot noise, and the laser beat note instability. However, measurements accurate to a half millimeter are possible despite these limitations. At present, measurements have only been taken over a few meters. However long-range measurements over several hundred meters could be possible with the same accuracy.

A possible modification of the system is proposed. A method of stabilizing a He-Ne laser and incorporating the system into the ranging unit is described. Increased accuracy is achieved and the remaining error is attributed to the shot noise in the photomultiplier.

The experimental system developed and checked in this report represents a possible substitute for presently used optical ranging methods. Present applications to which this system can be adapted include parabolic contour confirmation of tracking antennas used in the present space program.

PART V
LITERATURE CITED

1. AGA Corporation of America. Geodimeter: Model 4-D, 1964.
2. Cutler-Hammer AIL Division. Type 169 Laser Interferometer. Temporary Bulletin 60169 C-2, 1964.
3. Goldick, H. D. Frequency Stabilization of Double-Mode Gas Laser. Proceedings of the IEEE. 53, no. 6, p. 638. 1965.
4. Jaffe, Bernard. A Primer on Ferroelectricity and Piezoelectric Ceramics. Clevite Electronic Components Technical Paper TP-217, p. 4, 1960.
5. Jenkins, Francis and White, Harvey. Fundamentals of Optics. New York, McGraw-Hill, 1957. p. 245.
6. McAvoy, Nelson. 10.6 Micron System. Goddard Document X-524-65-461, p. 4, 1965.
7. Meade, Buford. Comparison Tests of Electro-Optical And Microwave Distance Measuring Instruments. Fourth United Nations Regional Cartographic Conference for Asia and the Far East, p. 19, 1964.
8. Plotkin, Henry H. Laser Communications Systems. Reports for UCLA Lectures, 1965.
9. Schwarz, Mischa. Information Transmission, Modulation, and Noise. New York, McGraw-Hill, 1959. p. 205.

10. Sinclair, Douglas and Givens, Parker. Determination of the Velocity of Light Using the Laser as a Source. Journal of the Optical Society of America. 56, no. 6, p. 795, 1964.
11. Troup, Gordon. Masers and Lasers. New York, Wiley, 1963. p. 150-152.
12. White, A. D. Frequency Stabilization of Gas Lasers. IEEE Journal of Quantum Electronics. QE-1, no. 8, pp. 349-350, 1965.